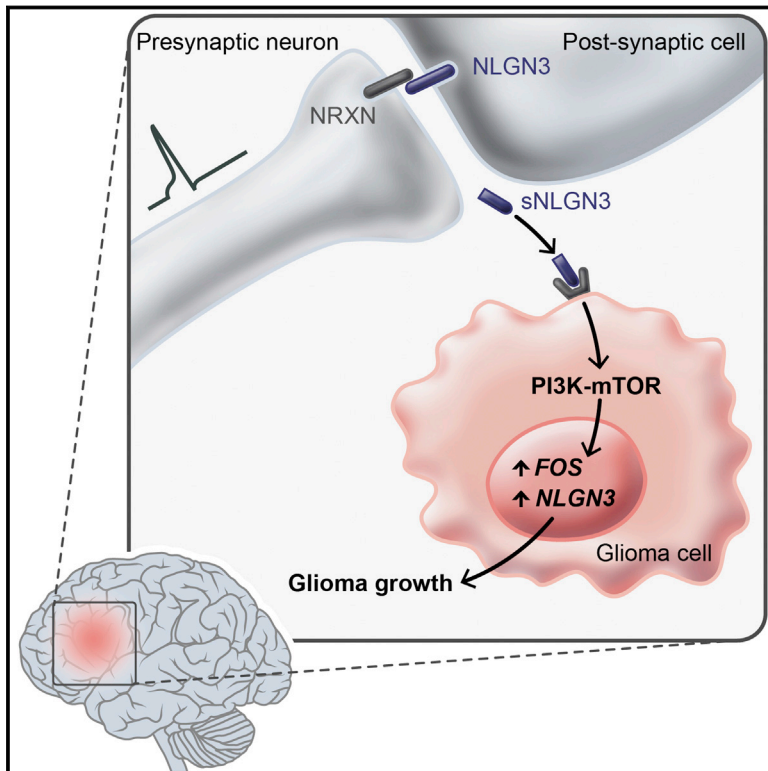


# Neuronal Activity Promotes Glioma Growth through Neuroligin-3 Secretion

## Graphical Abstract



## Authors

Humsa S. Venkatesh, Tessa B. Johung, ..., Parag Mallick, Michelle Monje

## Correspondence

mmonje@stanford.edu

## In Brief

Neuronal activity promotes the growth of malignant glioma through activity-regulated secretion of the synaptic protein neuroligin-3, which acts as a mitogen, recruiting the PI3K-mTOR pathway to induce glioma cell proliferation.

## Highlights

- Neuronal activity promotes high-grade glioma (HGG) proliferation and growth
- Neuroligin-3 is an activity-regulated secreted glioma mitogen
- Neuroligin-3 induces PI3K-mTOR signaling in HGG cells
- Neuroligin-3 expression is inversely correlated with survival in human HGG

## Accession Numbers

GSE62563

# Neuronal Activity Promotes Glioma Growth through Neuroligin-3 Secretion

Humsa S. Venkatesh,<sup>1,2,3,4,5,9</sup> Tessa B. Johung,<sup>1,2,3,4,5,9</sup> Viola Caretti,<sup>1,2,3,4,5,9</sup> Alyssa Noll,<sup>1,2,3,4,5</sup> Yujie Tang,<sup>1,2,3,4,5</sup> Surya Nagaraja,<sup>1,2,3,4,5</sup> Erin M. Gibson,<sup>1,2,3,4,5</sup> Christopher W. Mount,<sup>1,2,3,4,5</sup> Jai Polepalli,<sup>6</sup> Siddhartha S. Mitra,<sup>5</sup> Pamelyn J. Woo,<sup>1,2,3,4,5</sup> Robert C. Malenka,<sup>6</sup> Hannes Vogel,<sup>1,2,3,4</sup> Markus Bredel,<sup>7</sup> Parag Mallick,<sup>8</sup> and Michelle Monje<sup>1,2,3,4,5,\*</sup>

<sup>1</sup>Department of Neurology

<sup>2</sup>Department of Pediatrics

<sup>3</sup>Department of Pathology

<sup>4</sup>Department of Neurosurgery

<sup>5</sup>Institute for Stem Cell Biology and Regenerative Medicine

<sup>6</sup>Nancy Pritzker Laboratory, Department of Psychiatry and Behavioral Sciences  
Stanford University School of Medicine, Stanford, CA 94305, USA

<sup>7</sup>Department of Radiation Oncology, University of Alabama at Birmingham School of Medicine, Birmingham, AL 35233, USA

<sup>8</sup>Department of Radiology, Stanford University School of Medicine, Stanford, CA 94305, USA

<sup>9</sup>Co-first author

\*Correspondence: [mmonje@stanford.edu](mailto:mmonje@stanford.edu)

<http://dx.doi.org/10.1016/j.cell.2015.04.012>

## SUMMARY

Active neurons exert a mitogenic effect on normal neural precursor and oligodendroglial precursor cells, the putative cellular origins of high-grade glioma (HGG). By using optogenetic control of cortical neuronal activity in a patient-derived pediatric glioblastoma xenograft model, we demonstrate that active neurons similarly promote HGG proliferation and growth in vivo. Conditioned medium from optogenetically stimulated cortical slices promoted proliferation of pediatric and adult patient-derived HGG cultures, indicating secretion of activity-regulated mitogen(s). The synaptic protein neuroligin-3 (NLGN3) was identified as the leading candidate mitogen, and soluble NLGN3 was sufficient and necessary to promote robust HGG cell proliferation. NLGN3 induced PI3K-mTOR pathway activity and feedforward expression of *NLGN3* in glioma cells. *NLGN3* expression levels in human HGG negatively correlated with patient overall survival. These findings indicate the important role of active neurons in the brain tumor microenvironment and identify secreted NLGN3 as an unexpected mechanism promoting neuronal activity-regulated cancer growth.

## INTRODUCTION

High-grade gliomas (HGG), the leading cause of brain tumor death in both children and adults, occur in a striking spatiotemporal pattern highlighting the critical importance of the tumor microenvironment. Molecularly defined subtypes of HGG parse by neuroanatomical site of origin and patient age, with pontine

and thalamic HGGs typically occurring in mid-childhood, cortical gliomas of childhood occurring in older children and young adults, and HGG of later adulthood occurring chiefly in the frontotemporal lobes (Khuong-Quang et al., 2012; Schwartzentruber et al., 2012; Sturm et al., 2012; Wu et al., 2012). These age and neuroanatomical predilections of gliomagenesis point to interactions between cell of origin and microenvironment, suggesting dysregulation of neurodevelopment and/or plasticity.

Microenvironmental determinants of glioma cell behavior are incompletely understood, although important relationships between glioma cells and neighboring microglia, astrocytes, and vascular cells have recently come to light (Charles et al., 2011; Pyonteck et al., 2013; Silver et al., 2013). While cellular origins of HGG remain unclear, converging evidence implicates oligodendroglial precursor cells (OPCs) and earlier neural precursor cells (NPCs) as putative cells of origin for many forms of HGG (Galvao et al., 2014; Liu et al., 2011; Monje et al., 2011; Wang et al., 2009). Clues to microenvironmental influences driving HGG growth may thus be inferred from mechanisms governing the proliferation of normal NPCs and OPCs in the postnatal brain. We recently demonstrated that neuronal activity exerts a strong mitogenic effect on normal NPCs and OPCs in juvenile and adult mammalian brains (Gibson et al., 2014), raising the possibility that neuronal activity could promote proliferation in HGG.

## RESULTS

### Optogenetic Control of Cortical Neuronal Activity in a Patient-Derived Pediatric Cortical HGG Orthotopic Xenograft Model

To test the role of neuronal activity in HGG growth, we employed in vivo optogenetic stimulation of premotor cortex in freely behaving mice bearing patient-derived orthotopic xenografts of pediatric cortical glioblastoma (GBM; Figure 1A–1C). The well-characterized Thy1::ChR2 mouse model expressing the excitatory opsin channelrhodopsin-2 (ChR2) in deep cortical

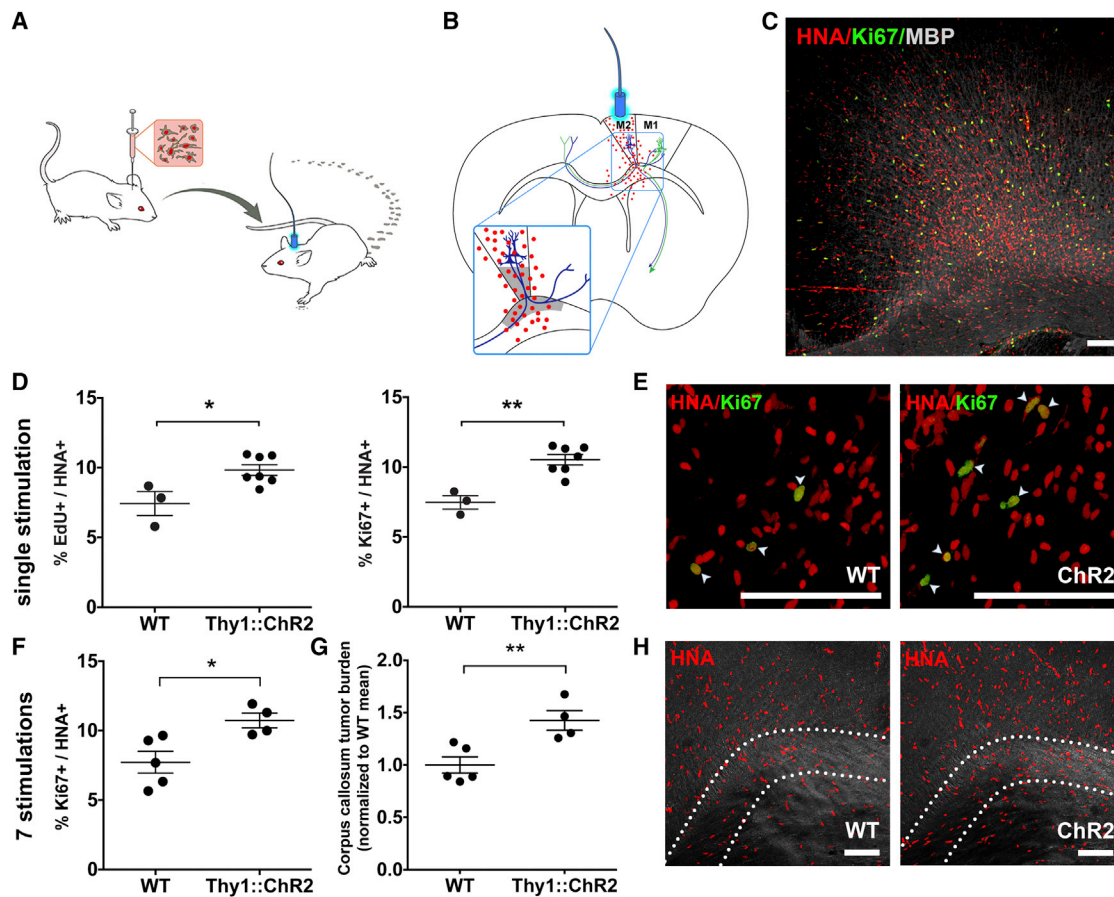


**Figure 1. Neuronal Activity Promotes High-Grade Glioma Proliferation and Growth In Vivo**

(A) In vivo optogenetic high-grade glioma (HGG) orthotopic xenograft model. (B) Schematic illustration of the optogenetically stimutable premotor circuit. Thy1::ChR2<sup>+</sup> premotor cortex (M2) neurons depicted in blue; primary motor cortex (M1) projection neurons, green; tumor cells depicted as red dots. Gray shading indicates region of analysis. (C) Confocal micrograph of infiltrating pHGG (SU-pcGBM2) cells expressing human nuclear antigen (HNA, red), proliferation marker Ki67 (green) in premotor cortical deep layers and subjacent corpus callosum (MBP, white). (D and E) Single optogenetic stimulation session paradigm. (D) Proliferation index of pHGG cells in identically manipulated WT;NSG (n = 3) and Thy1::ChR2;NSG (n = 7) mice, measured by the proportion of HNA<sup>+</sup> cells expressing EdU (left graph) or Ki67 (right graph) 24 hr after one optogenetic stimulation session. (E) Confocal micrograph illustrating proliferating (Ki67<sup>+</sup>, green) pHGG cells (HNA<sup>+</sup>, red) xenografted in WT;NSG (“WT”; left) or Thy1::ChR2;NSG mice (“ChR2”; right). (F–H) Repetitive optogenetic stimulation sessions paradigm. Xenografted WT;NSG (n = 5) and Thy1::ChR2;NSG (n = 4) mice evaluated 48 hr after seven daily sessions of optogenetic stimulation. (F) Proliferation index (Ki67<sup>+</sup>/HNA<sup>+</sup>) as in (D) above after seven stimulations. (G) Tumor cell burden increases following 1 week of brief daily optogenetic stimulation sessions, measured as HNA<sup>+</sup> cell density within the region of corpus callosum containing active premotor projections; data normalized to WT mean. (H) Confocal micrographs with differential interference contrast (DIC) background to illustrate regional tissue architecture; HNA<sup>+</sup> pHGG cells (red) are infiltrating premotor cortex and subjacent corpus callosum. Dotted line indicates region of analysis in corpus callosum. Data shown as mean ± SEM. \*p < 0.05, \*\*p < 0.01 by unpaired two-tailed Student’s t test. Scale bars, 100 μm. See also [Figure S1](#) and [Movie S1](#).

projection neurons (Arenkiel et al., 2007; Wang et al., 2007) was crossed onto an immunodeficient background (NOD-SCID-IL2R γ-chain-deficient, NSG), resulting in a mouse model (Thy1::ChR2;NSG) amenable to both in vivo optogenetics and orthotopic xenografting. ChR2-expressing neurons respond with action potentials to 473 nm light pulses with millisecond precision (Arenkiel et al., 2007; Boyden et al., 2005; Wang et al., 2007). Expression of ChR2 does not alter membrane properties in the absence of light or neuronal health in the absence or presence of light under established experimental conditions (Boyden et al., 2005). When an optical fiber is placed just below the pial surface (Figure 1B), ~10% of the irradiance penetrates midway

through cortex, thus stimulating the apical dendrites of deep cortical projection neurons expressing ChR2 (Yizhar et al., 2011). Stimulating the premotor circuit unilaterally at 20 Hz, consistent with the 10–40 Hz physiological firing rate of motor cortex projection neurons, elicits complex motor behavior (unidirectional ambulation; Arenkiel et al., 2007; Gibson et al., 2014; Wang et al., 2007). Optogenetic stimulation of the premotor circuit elicits a substantial increase in NPC and OPC proliferation (Gibson et al., 2014). At baseline, precursor cell proliferation is equivalent in mice expressing or lacking ChR2 (Gibson et al., 2014). In this experimental paradigm, the microglial inflammatory response to superficial fiber placement and subsequent light

stimulation is minimal in deep cortex, where ChR2-expressing neurons reside, resolves within days, and is equal in Thy1::ChR2 mice and identically manipulated wild-type (WT) controls (Gibson et al., 2014).

To develop an orthotopic xenograft model appropriate to the juvenile premotor cortex, a culture was established from pre-treatment biopsy tissue of a frontal cortex GBM (WHO grade IV) from a 15-year-old male (culture designated SU-pcGBM2; clinical characteristics, genomic characterization and DNA fingerprinting described in Table S1). These pediatric cortical HGG (pHGG) cells were xenografted unilaterally into premotor (M2) cortex of juvenile Thy1::ChR2;NSG mice, resulting in diffusely infiltrating glioma cells throughout premotor cortex and subjacent corpus callosum (Figure 1C). WT (no opsin) littermate control NSG mice (WT;NSG) were identically manipulated for comparison. After tumors were allowed to engraft for 2 months, an optical-neural interface was placed ipsilateral to the xenograft. The unilateral premotor cortex was optogenetically stimulated (473 nm, 20 Hz; cycles of 30 s on/90 s off over 30 min) in awake mice, resulting in unidirectional ambulation. pHGG xenografts did not impede the behavioral response to evoked premotor circuit activity (Movie S1). Light stimulation had no behavioral effect in identically manipulated xenografted WT;NSG mice. Mice were given one dose of EdU to label proliferating cells at the time of optogenetic manipulation and were sacrificed 24 hr later to examine acute effects of neural activity.

### Neuronal Activity Promotes High-Grade Glioma Growth In Vivo

Tumor cell burden and distribution did not differ between groups at the time of stimulation ( $p = 0.74$ ; Figures S1A and S1B). Xenografted human tumor cells (human nuclear antigen, HNA<sup>+</sup>) co-expressing EdU indicate glioma cells proliferating at the time of EdU administration and optogenetic stimulation, while co-expression of Ki67 indicates cells proliferating at the time of sacrifice 24 hr later. Within the premotor circuit (Figures 1B and S1C), the proliferation index of human tumor cells was increased in optogenetically stimulated Thy1::ChR2;NSG mice compared to that of identically manipulated WT mice, measured both as the percent of tumor cells co-expressing EdU ( $9.83\% \pm 0.38\%$  versus  $7.43\% \pm 0.86\%$ ;  $n = 7$  Thy1::ChR2;NSG mice,  $n = 3$  WT;NSG mice, respectively;  $p < 0.05$ ; Figures 1D and 1E) or co-expressing Ki67 ( $10.53\% \pm 0.37\%$  versus  $7.48\% \pm 0.48\%$ ;  $n = 7$  Thy1::ChR2;NSG mice,  $n = 3$  WT;NSG mice, respectively;  $p < 0.01$ , Figures 1D and 1E). This range of observed proliferation indices is consistent with that of human glioma. Proliferation index is typically  $<5\%$  for low-grade astrocytomas,  $5\%–15\%$  for anaplastic astrocytomas (WHO grade III), and  $10\%–20\%$  for GBMs (WHO grade IV); proliferation indices correlate inversely with prognosis, with those above  $10\%$  generally indicating poor prognosis (Johannessen and Torp, 2006). The observed activity-regulated increase in proliferation was restricted to the active circuit; in the prefrontal cortex, a region infiltrated by glioma cells but outside of the area stimulated by light, glioma cell proliferation indices were equivalent in Thy1::ChR2;NSG and WT;NSG mice (Figures S1D and S1E). While proliferation increased within the active circuit, glioma cell death remained

constant, with only rare tumor cells expressing cleaved caspase-3 in either group (Figures S1F and S1G).

A simplified Galton-Watson mathematical model (Gerlee, 2013) of tumor cell growth incorporating the neuronal activity-associated increase in proliferation index ( $b$ ) and a fixed cell death rate ( $d$ ) would predict an exponential growth effect of elevated neuronal activity within the active circuit ( $x_t = x_0(1+(b-d))^t$ ). Such a model utilizing the observed proliferation indices predicts an activity-regulated  $\sim 25\%$  increase in tumor cell number after seven cell divisions and  $\sim 50\%$  tumor increase after 14 divisions. To test this prediction in vivo, we utilized a repetitive stimulation paradigm in which mice were optogenetically manipulated as above for 10 min daily on 7 consecutive days and were sacrificed 48 hr after the final session. Following repetitive elevations in premotor circuit activity, tumor cell proliferation index was increased in xenografted Thy1::ChR2;NSG mice to a similar degree as in the single optogenetic stimulation paradigm ( $10.74\% \pm 0.61$  versus  $7.72\% \pm 0.88$ ;  $n = 4$  Thy1::ChR2;NSG mice,  $n = 5$  WT;NSG mice;  $p < 0.05$ , Figure 1F). As predicted, periodically elevated neuronal activity for 1 week yielded a  $\sim 42\%$  increase in tumor cell burden within the active circuit relative to identically manipulated WT controls ( $n = 4$  Thy1::ChR2;NSG,  $n = 5$  WT;NSG mice;  $p < 0.01$ ; Figures 1G and 1H). These data reflect the influence of neuronal activity on tumor burden during the exponential growth phase; over the course of the disease, as disruption of healthy tissue progresses and the microenvironment evolves, the effects of neuronal activity on glioma growth could change.

### Neuronal Activity Promotes Glioma Proliferation through Secreted Factors

To determine whether neurons stimulate glioma proliferation via secretion of an activity-regulated mitogen(s), we optogenetically stimulated acute cortical slices from Thy1::ChR2 or identically manipulated WT mice in situ and collected the conditioned medium (CM), to which we exposed patient-derived HGG cultures (Figure 2A). The slice stimulation paradigm mirrored the in vivo paradigm, using 473 nm light at 20 Hz for cycles of 30 s on, 90 s off over a 30 min period. For this in situ optogenetic model, expected neuronal firing in response to light was validated electrophysiologically, confirming 20 Hz spike trains for 30 s periods throughout the 30 min session (Figure 2B). Maintenance of slice health throughout this paradigm was confirmed electrophysiologically and histologically (Figures S2A–S2D). Cortical slices from WT mice were identically manipulated for comparison. In parallel, CM was collected from blue light-unexposed Thy1::ChR2 and WT cortical slices. Patient-derived HGG cultures were then placed in CM from stimulated (light-exposed) or unstimulated cortical slices (Figure 2A). The HGG cell proliferation index (fraction of total cells in S phase as detected by EdU incorporation) was determined after 24 hr exposure to CM from the acute cortical slice conditions described above. The CM from optogenetically stimulated Thy1::ChR2 cortical slices (active CM) increased the in vitro proliferation index of pHGG (SU-pcGBM2) cells in comparison to CM from all control conditions, including identically manipulated WT, unstimulated Thy1::ChR2, or unstimulated WT cortical slices, or in comparison to blue light-exposed or non-exposed aCSF medium lacking

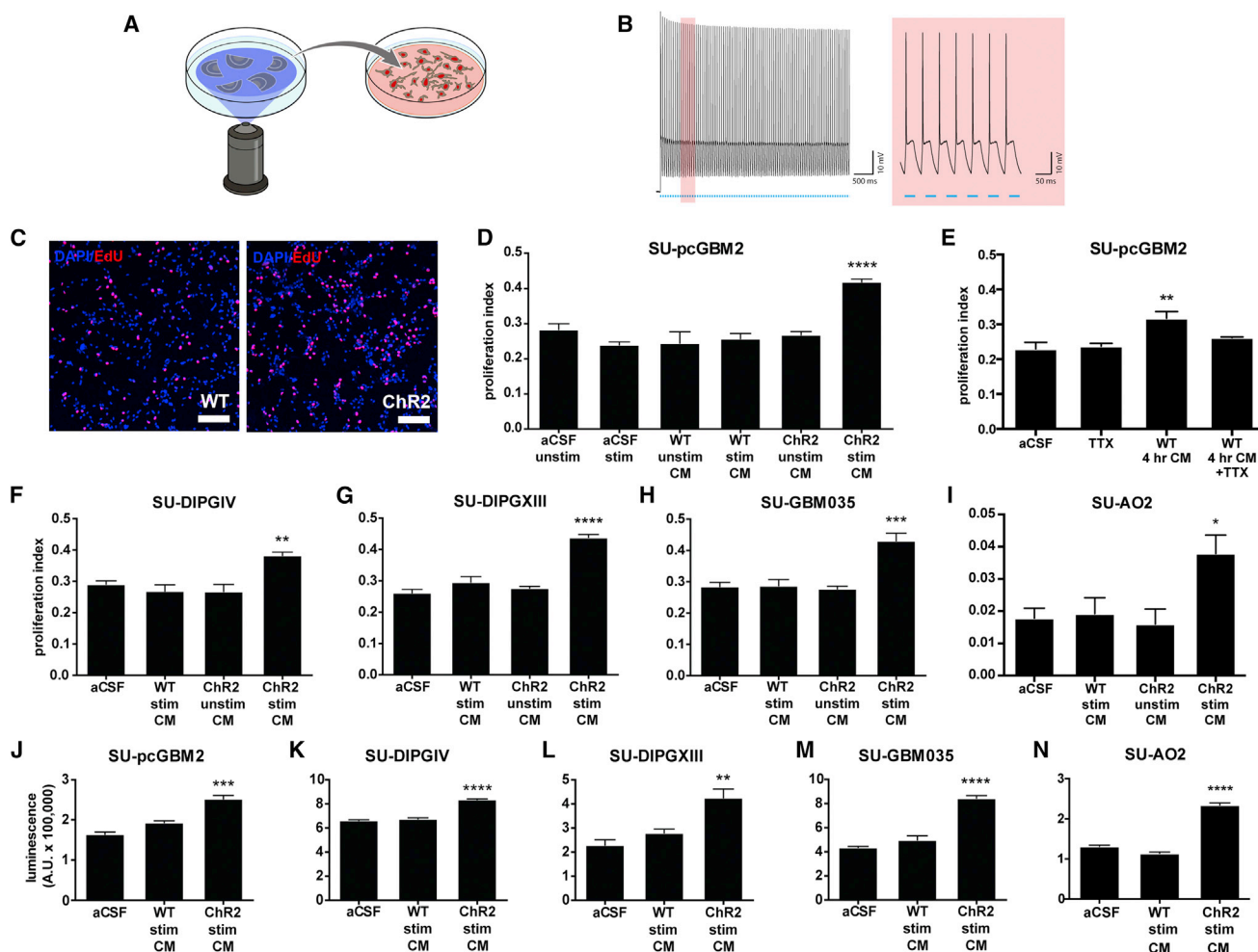


**Figure 2. Activity-Regulated Secreted Factors Promote Glioma Cell Proliferation**

(A) Schematic depicts optogenetic stimulation of acute cortical slices and collection of conditioned medium (CM). (B) Electrophysiological demonstration by patch-clamp recording (left; trace highlighted in red is magnified at right) of 20 Hz neuronal firing in response to 20 Hz blue light pulses throughout the 30 s stimulation period in the Thy1::ChR2 cortical slice. (C) Representative confocal micrographs show increased uptake of EdU (red) in cells (DAPI, blue) exposed to CM from stimulated Thy1::ChR2 slices (active CM) versus those exposed to CM from blue light-exposed WT slices (WT CM). (D) Proliferation index of SU-pcGBM2 cells exposed to optogenetically stimulated or unstimulated Thy1::ChR2 cortical slice CM (“WT stim CM”) or non-exposed WT cortical slice CM (“WT unstim CM”), or plain media (aCSF). (E) Proliferation index of SU-pcGBM2 cells after exposure to CM generated from light-unexposed WT slice conditioning for 4 hr in the presence or absence of 1  $\mu$ M tetrodotoxin (TTX). (F–I) Active CM similarly increased the proliferation index of DIPG (F and G), adult GBM (H), and anaplastic oligodendroglioma (I) cultures. (J–N) Active CM increased the viable cell number measured by CellTiter-Glo after 72 hr of incubation with active or light-exposed WT CM in pediatric and adult GBM (J and M), DIPG (K and L), and anaplastic oligodendroglioma (N) cells. All experiments analyzed by one-way ANOVA and performed with  $n = 3$  biological replicates. Data shown as mean  $\pm$  SEM. \* $p < 0.05$ , \*\* $p < 0.01$ , \*\*\* $p < 0.001$ , \*\*\*\* $p < 0.0001$ . Scale bars, 100  $\mu$ m. See also Figure S2 and Table S1.

slices ( $F = 15.49$ ,  $p < 0.0001$ ; Figures 2C and 2D). Active CM did not alter glioma cell death, as assessed by Annexin V FACS analysis (Figure S2E). The secretion of activity-regulated mitogen(s) was not frequency dependent, as CM from Thy1::ChR2 cortical slices optogenetically stimulated at 5 Hz elicited the same proliferative effect on pHGG cells (Figure S2F).

WT cortical slices do exhibit spontaneous neuronal activity; thus, we expect activity-regulated secreted factors to be present in WT CM, albeit to a lesser extent than in media conditioned by

Thy1::ChR2 slices with optogenetically elevated neuronal activity. To further explore the possible effects of spontaneous activity, we allowed WT slices to condition the media without blue light for 4 hr rather than 30 min in the presence or absence of the specific voltage-gated sodium channel blocker tetrodotoxin (TTX) to silence spontaneous action potentials. WT CM conditioned for a longer duration elicited an increase in pHGG proliferation; this effect was blocked in CM from slices incubated with TTX (proliferation index  $0.32 \pm 0.03$  with 4 hr WT CM exposure

versus  $\sim 0.25$  with aCSF, aCSF + TTX, or WT CM + TTX exposure;  $F = 8.45$ ;  $p < 0.01$ ; [Figure 2E](#)). Together, these data indicate that spontaneous neuronal activity regulates secretion of a glioma mitogen(s).

To determine whether this proliferative response to activity-regulated secreted factor(s) was specific to the pHGG model (SU-pcGBM2 cells) or more broadly applicable, we tested nine additional patient-derived HGG cell cultures ([Table S1](#)). All four tested cultures of diffuse intrinsic pontine glioma (DIPG), the most common form of pediatric HGG, demonstrated a similarly robust proliferative response to active CM exposure ([Figures 2F, 2G, S2G, and S2H](#)). We next tested four patient-derived adult GBM cultures and found a similar increase in cell proliferation after exposure to active CM ([Figures 2H, S2I, and S2J](#)) in all but one, which was a young adult epithelioid *BRAF*<sup>V600E</sup> mutant GBM (SU-GBM047; [Figure S2K](#)). As the mitogenic effect appears largely generalizable across distinct HGG classes, we also tested a patient-derived culture of adult anaplastic oligodendroglioma and similarly observed increased cell proliferation in response to activity-regulated secreted factors ([Figure 2I](#)). Consistent with spontaneous neuronal activity of WT slices, some cultures exhibit a small but significant increase in proliferation in response to WT CM (e.g., SU-DIPGVI, proliferation index  $0.21 \pm 0.01$  in aCSF versus  $0.31 \pm 0.02$  in WT CM versus  $0.46 \pm 0.002$  in active CM; [Figures S2G and S2J](#)).

To ascertain whether the observed effect indicated an increase in overall glioma growth, we used the quantitative viable cell assay CellTiter-Glo following 72 hr exposure to cortical slice CM and found an increase in viable HGG cell number when cultures were exposed to active CM ([Figures 2J–2N and S2L–S2N](#)).

### Activity-Regulated Glioma Mitogen(s) Are Secreted Proteins

A series of biochemical analyses was employed to ascertain the nature of the activity-regulated mitogen(s). To determine whether the mitogen(s) are small molecules or macromolecules, active or control CM was collected as above and fractionated by molecular size. The  $>10$  kDa macromolecular fraction of active CM, but not the  $<10$  kDa fraction, increased the in vitro glioma proliferation index ([Figure 3A](#)). Subsequent fractionation indicated that the mitogen(s) were present in the  $<100$  kDa fraction ([Figure 3B](#)). To determine the biochemical nature of the mitogen(s), active CM was heated to  $>100^\circ\text{C}$  to denature proteins, resulting in loss of its mitogenic effect ([Figure 3C](#)). In contrast, treatment of active CM with RNase and DNase had no effect on its proliferation-inducing capacity ([Figure 3D](#)). Taken together, these data indicate that the neuronal activity-regulated secreted mitogen(s) is a protein between 10–100 kDa.

With respect to small molecules, high levels of glutamate release into CM would not be expected in a healthy brain slice, as perisynaptic astrocytes take up released glutamate from the synaptic cleft ([Rothstein et al., 1996](#)). Indeed, low levels of glutamate were present in active CM ([Figure S3A](#)). Thus, this in situ experimental paradigm does not address the potential role of glutamate in neuronal activity-regulated glioma cell proliferation in vivo.

### Cortical Projection Neuronal Activity-Regulated Secretome

To identify the secreted protein(s) that increase glioma cell proliferation in an activity-dependent manner, we employed mass spectrometric analyses of the cortical slice CM. Of note, neuronal activity may regulate secretion of proteins from neurons themselves or from other cell types in response to active neurons. Active CM and light-exposed WT CM were analyzed and compared using 2D gel electrophoresis to separate the secreted proteins by size and charge; differentially secreted protein spots were then identified by mass spectrometry. The 2D gel analyses were performed in duplicate using independent samples ([Figure 3E](#)). Quantitative mass spectrometric techniques of spectral counting and tandem mass tags (TMT) were then used with a third set of independent samples to confirm the 2D gel results and to more precisely define the absolute and relative quantities of each protein in the CM samples. The intersection of these analyses most consistently and robustly identified neuroligin-3 (Nlgn3) as the leading candidate mitogen ([Figure 3F](#)), present in active CM at a concentration of  $\sim 20$ – $40$  nM and upregulated by 2.6-fold compared to light-exposed WT CM. Additional candidates identified are listed in [Figure 3G](#).

The neuroligins are a family of synaptic proteins with a large N-terminal ectodomain, single pass transmembrane domain, and smaller C-terminal cytoplasmic domain ([Südhof, 2008](#)). Neuroligin-1 (Nlgn1), acting primarily at excitatory synapses similarly to Nlgn3, is secreted in an activity-regulated fashion by enzymatic cleavage of the N-terminal ectodomain ([Peixoto et al., 2012](#); [Suzuki et al., 2012](#)). The 2D gel and quantitative mass spectrometric analyses across all three independent samples demonstrated excellent coverage of the Nlgn3 ectodomain amino acid sequence (protein prophet score = 1; [Table S2](#)), identifying the protein with high confidence ([Figure 3H](#)). However, the C-terminal transmembrane and cytoplasmic domain of the protein was not detected in Nlgn3 isolated from the active CM ([Figure 3H](#)).

### Secreted Neuroligin-3 Promotes Glioma Cell Proliferation

The sufficiency of NLGN3 to promote HGG cell proliferation was then tested in vitro. We obtained recombinant full-length human NLGN3 and confirmed its identity and purity by mass spectrometry ([Figure S3B](#)). In contrast to the Nlgn3 present in the CM, mass spectrometric analysis of recombinant NLGN3 did identify peptide sequences within the C-terminal tail. 24 hr exposure of pHGG cells to recombinant NLGN3 at various concentrations in vitro promoted a significant increase in proliferation index ([Figure 4A](#)), with no change in cell death as measured by Annexin V FACS analysis ([Figure 4B](#)). NLGN3 at the concentration present in the active CM (20–40 nM) elicits an increase in proliferation commensurate with the effect of active CM ([Figures 4A and 2D](#)). NLGN3 promoted proliferation of each additional patient-derived cell culture tested, including DIPG, adult GBM, and anaplastic oligodendroglioma, with the exception of the epithelioid GBM culture ([Figures 4C and S4A](#)).

Additional candidates identified in the proteomic analyses above were also screened in pHGG cells in vitro. Of these, brain-derived neurotrophic factor (BDNF) and the known glioma

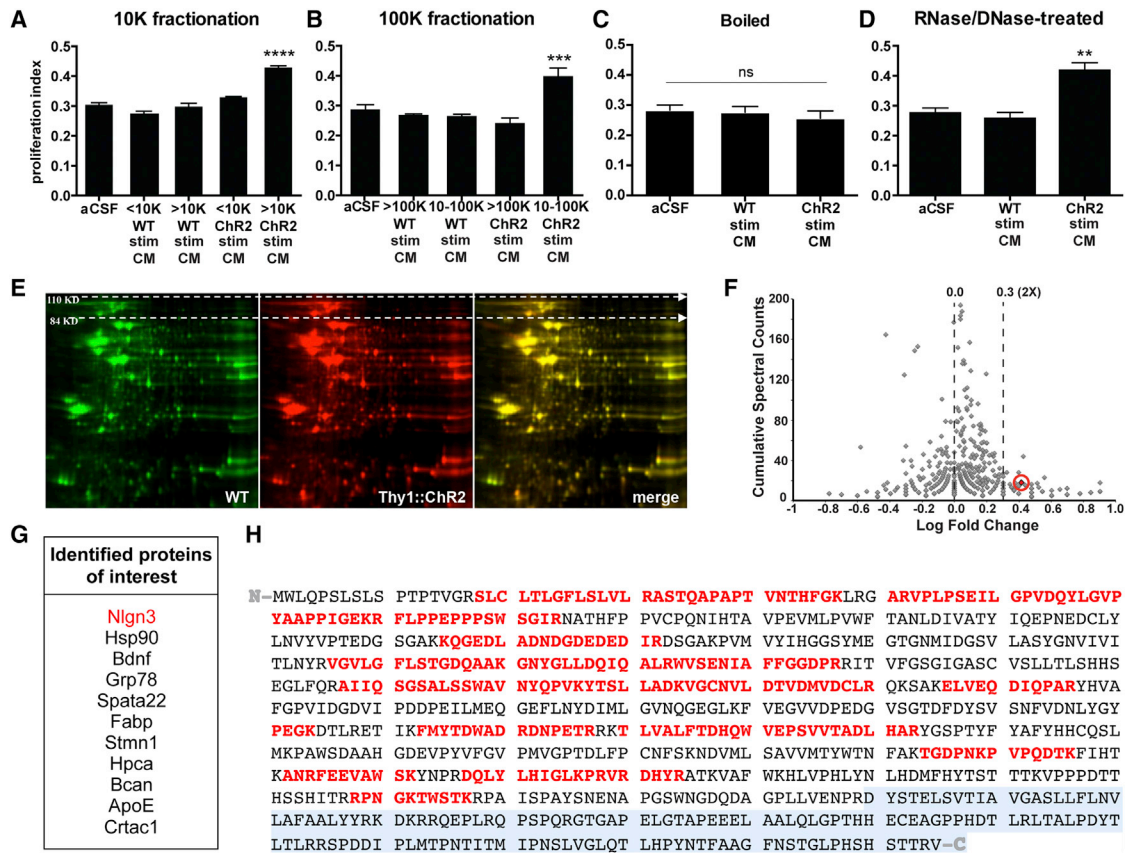


**Figure 3. Cortical Neuronal Activity-Regulated Glioma Mitogen(s) Are Protein(s)**

(A and B) Fractionation of CM by molecular size reveals that the activity-regulated mitogenic factors are >10 kDa (A) and <100 kDa (B). (C) Heating active CM to 100°C inactivates the mitogen(s). (D) RNA and DNA digestion of active CM does not change its mitogenic effect. All experiments analyzed by one-way ANOVA and performed with n = 3 biological replicates. Data shown as mean ± SEM. \*\*p < 0.01, \*\*\*p < 0.001, \*\*\*\*p < 0.0001. n.s. indicates p > 0.05. (E) Representative two-dimensional gel electrophoresis separating proteins in light-exposed WT CM (green) and active CM (red) by size (vertical axis) and charge (horizontal axis); merged images, right-most panel. (F) Volcano plot of spectral counting data shows the ratio of peptides in a given protein found in active CM versus CM from unstimulated Thy1::ChR2 slices. Neuroligin-3 (Nlg3) is highlighted and circled in red. (G) List of candidate proteins of interest identified from proteomic analyses. (H) Nlg3 peptide sequence. Peptides in red were identified by mass spectrometry of the Nlg3 isolated from active CM. Despite excellent coverage across the N-terminal ectodomain of the protein, no part of the C-terminal endodomain (transmembrane and intracellular domains, shaded gray) was identified in the isolated soluble Nlg3. See also Figure S3 and Table S2.

mitogen 78 kDa glucose-regulated protein (GRP78; Lee et al., 2008) promoted pHGG proliferation but less potently than NLGN3 (Figures S4B–S4D). Additional candidates tested did not affect proliferation, even at high concentrations (Figure S4B). Thus, NLGN3 emerged as an unexpected cortical neuronal activity-regulated glioma mitogen, together with known mitogens BDNF and GRP78.

To test the necessity of Nlg3 for the proliferation-promoting effect of active CM, we utilized the specific and avid binding of neurexin-1β (NRXN1β) to NLGN3 (Ichtchenko et al., 1996) to deplete Nlg3 from the cortical slice CM. Confirming that NRXN1β in this setting does deplete the available Nlg3, addition of NRXN1β completely abrogated the mitogenic effect of recombinant NLGN3 exposure (proliferation index 0.40 ± 0.01 in pHGG

cells exposed to 50 nM NLGN3 versus 0.28 ± 0.01 in cells exposed to 50 nM NLGN3 + 500 nM NRXN1β; p < 0.001; Figure 4D). Addition of NRXN1β alone to aCSF or to WT CM had no effect on proliferation index (Figure 4D). However, addition of NRXN1β significantly decreased the mitogenic effect of active slice CM on pHGG cells (proliferation index 0.40 ± 0.01 in cells exposed to active CM versus 0.34 ± 0.01 with exposure to active CM + NRXN1β; p < 0.05; Figure 4D), indicating that secreted NLGN3 is necessary for the full mitogenic effect of cortical neuronal activity on glioma cells. The incomplete abrogation of the mitogenic effect of the CM with addition of NRXN1β is consistent with additional activity-regulated glioma mitogens GRP78 and BDNF present in the CM (Figures S4B–S4D). Indeed, pharmacological inhibition of the BDNF receptor TRKB in

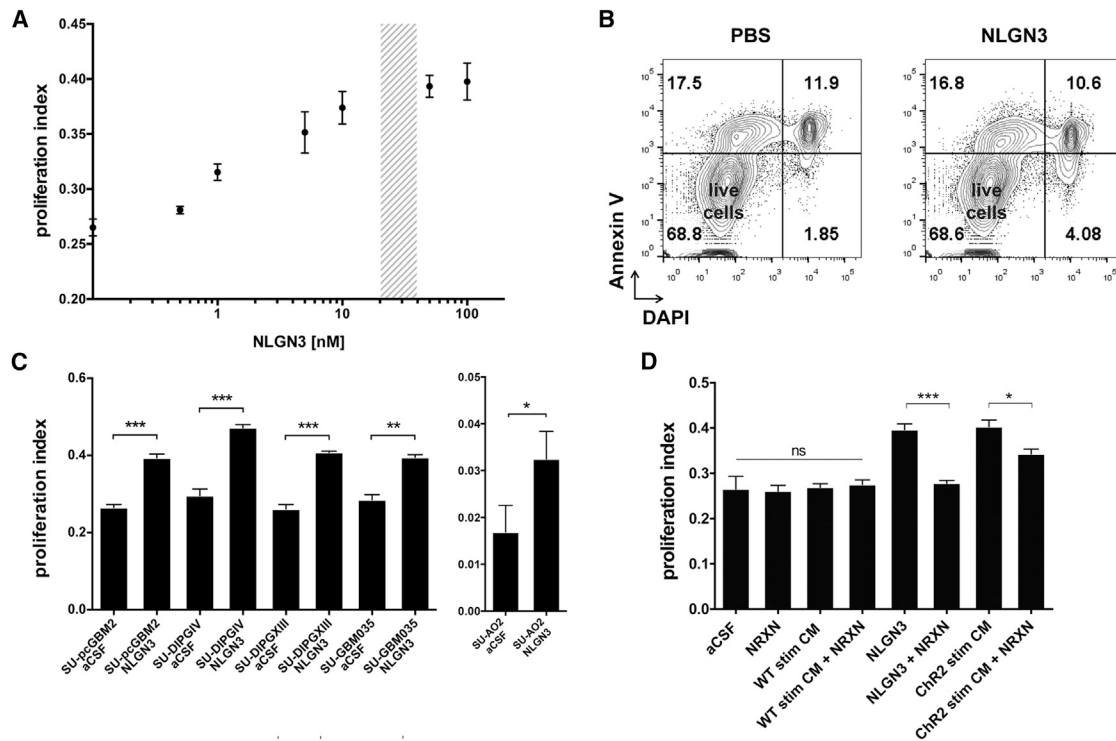


**Figure 4. Secreted Neuroligin-3 Mediates Neuronal Activity-Regulated Glioma Proliferation**

(A) Seven-point dose curve plots SU-pcGBM2 proliferation index as measured by EdU<sup>+</sup>/DAPI<sup>+</sup> staining 24 hr after exposure to recombinant NLGN3 at a 0–100 nM concentration range. Shaded region indicates concentration present in active CM. (B) After 24 hr exposure to PBS or NLGN3 (50 nM), SU-pcGBM2 cells were stained with DAPI (x axis) and Annexin V-FITC (y axis) to detect cell death by FACS analysis, performed in biological duplicate. Live Annexin V<sup>-</sup>/DAPI<sup>-</sup> cells shown in lower-left quadrant of contour plots; pre-apoptotic Annexin V<sup>+</sup>/DAPI<sup>-</sup> cells, left upper quadrant; dead Annexin V<sup>+</sup>/DAPI<sup>+</sup> cells, right upper quadrant. No increase in cell death was seen with NLGN3 exposure. (C) Proliferation indices of various patient-derived HGG cell lines exposed to 50 nM NLGN3 for 24 hr (unpaired two-tailed Student's t tests). (D) Neurexin-1β (NRXN, 500 nM), which binds NLGN3 with high affinity, effectively blocks the mitogenic effect of recombinant NLGN3 (50 nM) and abrogates the mitogenic effect of active CM (unpaired two-tailed Student's t tests). Exposure to NRXN alone or added to light-exposed WT CM ("WT Stim CM") does not affect pHGG cell proliferation (one-way ANOVA). For all experiments, n = 3 biological replicates unless otherwise noted. Data shown as mean ± SEM. \*p < 0.05, \*\*p < 0.01, \*\*\*p < 0.001. n.s. indicates p > 0.05. See also Figure S4.

combination with NRXN1β completely abrogated the proliferative effect of active CM (Figure S4E).

### Downstream Mechanisms of Neuronal Activity-Regulated Glioma Proliferation

To begin to understand the intracellular signaling mechanisms by which neuronal activity promotes HGG cell proliferation, we performed RNA sequencing to define the transcriptome of pHGG cells exposed to active CM versus light-exposed WT CM. Pathway analysis of differentially regulated genes revealed upregulation of the immediate early gene and proto-oncogene *FOS*, whose expression can be downstream of pathways that include PI3K-mTOR signaling or MAPK signaling (Greenberg and Ziff, 1984; Gonzales and Bowden, 2002; Chen and Davis, 2003), suggesting potential involvement of either pathway (Table S3). Exposure to NLGN3 similarly resulted in upregulation of *FOS* expression, determined by qPCR (Figure 5A). However, western blot analysis did not reveal upregulation of phospho-ERK1/2<sup>T202/Y204</sup>, an indicator of MAPK pathway activation, following NLGN3 exposure (Figures S5A and S5B). We thus

examined PI3K pathway recruitment by exposure to NLGN3 using western blot analysis of phospho-AKT<sup>S473</sup>; pHGG cells exposed to NLGN3 exhibited increased phospho-AKT<sup>S473</sup> levels relative to total AKT in a dose-dependent manner ( $F = 17.99$ ,  $p < 0.001$ ; Figure 5B-C). PI3K canonically regulates mammalian target of rapamycin (mTOR), and thus we examined the effect of NLGN3 exposure on mTOR activity using western blot analysis of phospho-4E-BP1<sup>T37/46</sup>, revealing an increase in phospho-4E-BP1<sup>T37/46</sup> relative to total 4E-BP1 following NLGN3 exposure (Figures 5D and 5E). Blockade of PI3K or mTOR pharmacologically or via shRNA-mediated knockdown prevented the NLGN3-mediated mitogenic effect (Figures 5F–5H and S5C–S5E). Neuronal activity-regulated secretion of NLGN3 thus recruits the PI3K-mTOR pathway to promote glioma cell proliferation.

Surprisingly, we also found upregulated expression of the neuroligin-3 gene (*NLGN3*) in pHGG cells exposed to active CM (Table S3), suggesting a positive feedforward effect on glioma cell *NLGN3* expression. To determine whether soluble NLGN3 exposure induces its own expression, we performed

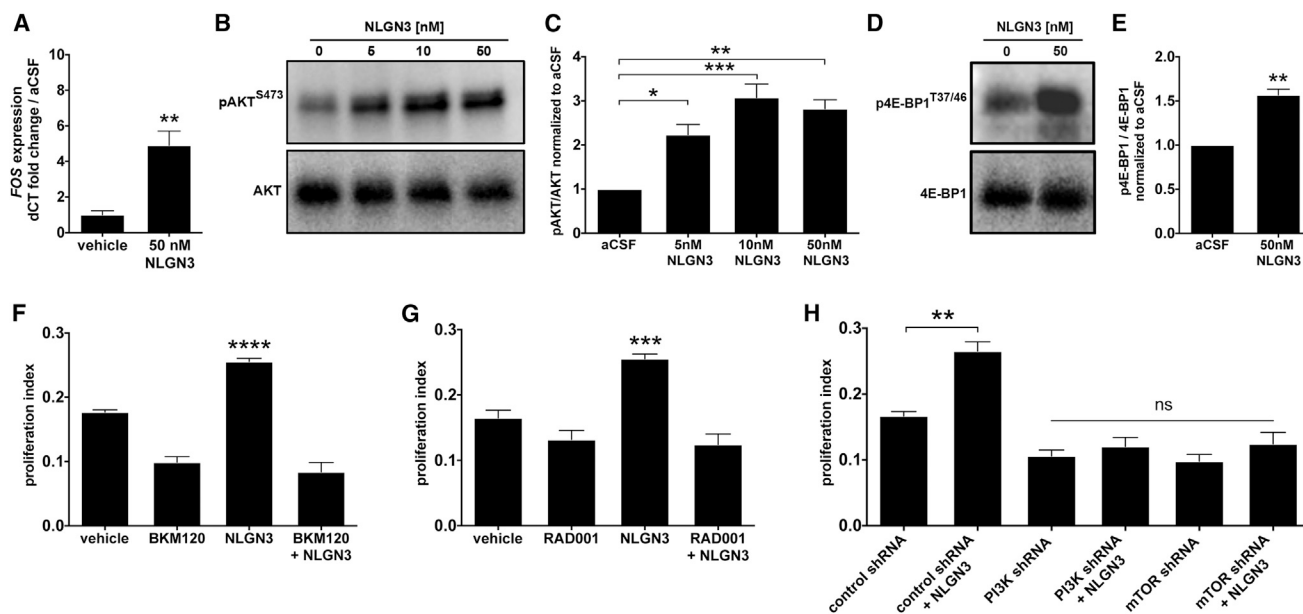


**Figure 5. Secreted Neuroligin-3 Recruits the PI3K Pathway and Promotes Feedforward Expression of NLGN3**

(A) FOS mRNA expression increases after 1 hr exposure to 50 nM NLGN3 compared to vehicle ( $p < 0.01$  by unpaired two-tailed Student's *t* test). (B) NLGN3 increases PI3K pathway signaling. Representative western blot shows increased phosphorylation of AKT (pAKT<sup>S473</sup>, top; total AKT, bottom) in response to NLGN3 concentrations ranging from 0 to 50 nM. (C) Quantification of the pAKT<sup>S473</sup>/AKT ratio fold change (normalized to aCSF) observed in (B). (D) Representative western blot demonstrates increased phosphorylation of 4E-BP1, a downstream reporter of mTOR, after 50 nM NLGN3 exposure. (Top) 4E-BP1<sup>T37/46</sup>, (bottom) total 4E-BP1. (E) Quantification of p4E-BP1<sup>T37/46</sup>/4E-BP1 ratio fold change after NLGN3 exposure normalized to aCSF control (unpaired two-tailed Student's *t* test). (F) 50 nM NLGN3-induced increase in SU-pcGBM2 proliferation index (EdU assay) is blocked by inhibition of PI3K by BKM120 (100 nM). (G) Similar to (F), inhibition of mTOR by RAD001 (100 nM) blocks 50 nM NLGN3-induced proliferation in SU-pcGBM2 cells. (H) Genetic knockdown using specific shRNA against either *PI3K* or *mTOR* blocks effect of 50 nM NLGN3 on proliferation index (EdU assay in SU-pcGBM2). \* $p < 0.05$ , \*\* $p < 0.01$ , \*\*\* $p < 0.001$ , \*\*\*\* $p < 0.0001$  by one-way ANOVA with Tukey's post hoc tests to further examine pairwise comparisons unless otherwise indicated. All experiments performed in  $n = 3$  biological replicates. Data shown as mean  $\pm$  SEM. See also Figure S5 and Table S3.

qPCR in cells exposed to recombinant NLGN3 and found that this elicits increased glioma cell *NLGN3* gene expression, tested in both pediatric cortical HGG ( $F = 9.70$ ,  $p < 0.01$ ; Figure 6A) and DIPG cells ( $F = 13.56$ ,  $p < 0.01$ ; Figure 6B). The role of PI3K-mTOR pathway activity in this positive feedforward effect was investigated using treatment with the PI3K inhibitor BKM120 or shRNA-mediated *PI3K* knockdown (Figures 6A–6D), both of which blocked the soluble NLGN3-induced increase in *NLGN3* gene expression (Figures 6A–6D and S6). Similarly, the mTOR inhibitor RAD001 or shRNA-mediated *mTOR* knockdown prevented the feedforward effect of NLGN3 on *NLGN3* gene expression (Figures 6C and 6E–6G). Soluble NLGN3 thus promotes glioma cell feedforward expression of *NLGN3* via the PI3K-mTOR pathway. To determine whether other ligands known to stimulate the PI3K pathway in glioma (Fan et al., 2009) similarly affect *NLGN3* expression, we tested the effect of epidermal growth factor (EGF) exposure on glioma cell *NLGN3* expression and found no effect ( $p = 0.781$ ; Figure 6H), suggesting that *NLGN3* expression is specific to the context of NLGN3 exposure. Protein expression of NLGN3 following glioma cell NLGN3 exposure was confirmed using western blot analysis; in contrast, glioma cell NLGN3 protein expression was not found at baseline culture conditions (Figure 6I). NLGN3 thus results in feedforward

expression at the transcriptional and translational levels. Together, these findings indicate that *NLGN3* expression is an indicator of neuronal activity-dependent NLGN3 signaling to glioma cells (Figure 6J).

### Neuroligin-3 Gene Expression Is Associated with Decreased Survival in Human High-Grade Glioma

Having demonstrated that NLGN3 exposure increases tumor cell *NLGN3* expression, we next asked whether the *NLGN3* gene exhibited aberrations in glioma. Analysis of data from The Cancer Genome Atlas (TCGA) showed that somatic mutations in *NLGN3* are infrequent in pediatric (pilocytic astrocytoma/medulloblastoma, 0.4%) and adult brain tumors (low-grade gliomas, 1.1%; high-grade gliomas, 0.4%; Table S4). Interestingly, an extended analysis of *NLGN3* mutations and copy-number aberrations across multiple cancer types in the International Cancer Genome Consortium (ICGC) and the cBioPortal for Cancer Genomics databases revealed more frequent mutations and amplifications in other tumors, with particular predominance in thyroid, pancreatic, prostate, and gastric cancers (Figure S7C and Table S4).

To validate the clinical significance of NLGN3 in human glioma pathophysiology, we next examined the relationship between

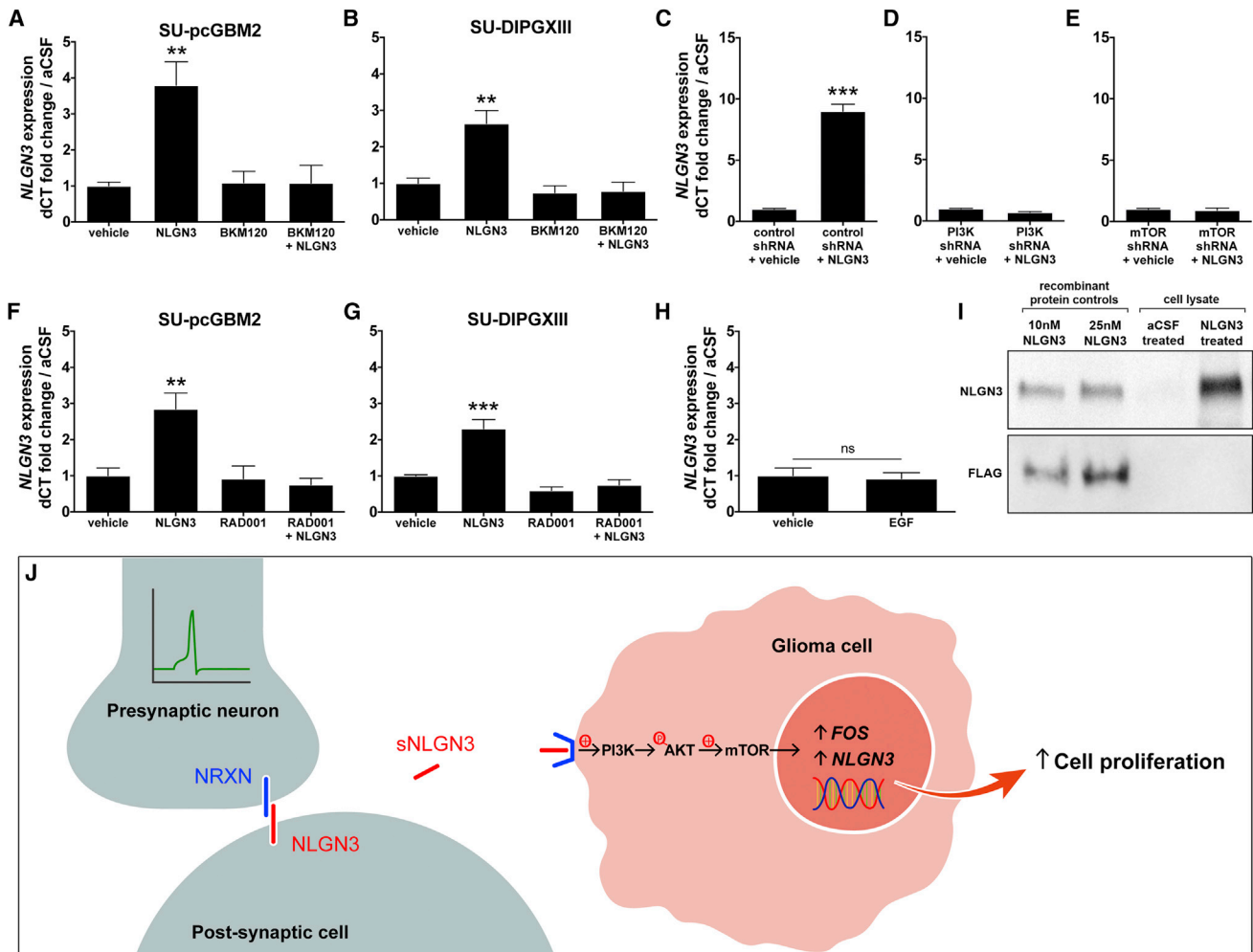
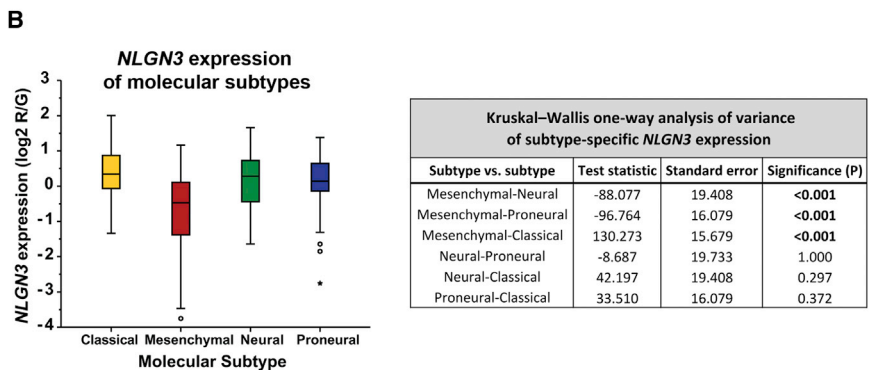
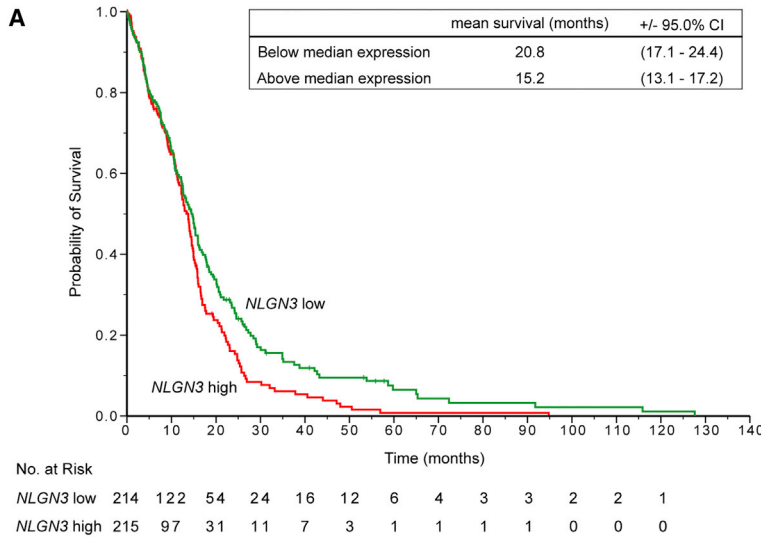


**Figure 6. Secreted Neuroligin-3 Promotes Feedforward Expression of *NLGN3* through Recruitment of the PI3K-mTOR Pathway**

(A) *NLGN3* mRNA expression in SU-pcGBM2 cells after 12 hr exposure to vehicle, 50 nM NLGN3, 100 nM BKM120, or 50 nM NLGN3 + 100 nM BKM120. (B) As in (A), SU-DIPGXIII *NLGN3* mRNA expression after exposure to NLGN3 and BKM120 alone or in combination. (C–E) *NLGN3* mRNA expression in SU-pcGBM2 cells after shRNA-mediated knockdown of either *PI3K* or *mTOR*. Only cells exposed to scrambled shRNA control exhibit increased *NLGN3* expression after NLGN3 exposure (unpaired two-tailed Student's *t* test.) (F) *NLGN3* mRNA expression in SU-pcGBM2 cells after 12 hr exposure to vehicle, 50 nM NLGN3, 100 nM RAD001, or 50 nM NLGN3 + 100 nM RAD001. (G) As in (F), SU-DIPGXIII *NLGN3* mRNA expression after exposure to NLGN3 and RAD001 alone or in combination. (H) *NLGN3* mRNA expression in SU-pcGBM2 cells does not change after 12 hr exposure to 50 nM EGF versus vehicle (unpaired two-tailed Student's *t* test). All qPCR data (A–H) are normalized to vehicle-treated samples and represent fold change of the delta CT in reference to  $\beta$ -actin. (I) Western blot analysis illustrating *NLGN3* protein expression. Lanes 1 and 2 = 10 nM and 25 nM recombinant FLAG-tagged *NLGN3*, respectively. Lanes 3 and 4 = lysate from SU-pcGBM2 cells exposed to aCSF or 50 nM recombinant FLAG-tagged *NLGN3*, respectively. Top panel probed with anti-*NLGN3*; bottom panel probed with anti-FLAG. (J) Schematic illustrating the model of neuronal activity-regulated *NLGN3* secretion from a post-synaptic cell, subsequent recruitment of glioma cell PI3K-mTOR pathway, expression of *FOS* and *NLGN3*, and proliferation. *n* = 3 biological replicates unless otherwise stated. Data shown as mean  $\pm$  SEM. \**p* < 0.05, \*\**p* < 0.01, \*\*\**p* < 0.001 by one-way ANOVA unless otherwise stated. n.s. indicates *p* > 0.05. See also Figure S6 and Table S3.

*NLGN3* gene expression and patient survival in 429 cases of adult GBM in TCGA. *NLGN3* mRNA expression level was found to be inversely correlated with patient overall survival (Figure 7). A two-class model in which patients were stratified according to median *NLGN3* expression showed an association between higher *NLGN3* expression and shorter survival (*p* < 0.05 by the log-rank test; Figure 7A). In patients whose tumors exhibited

below-median *NLGN3* expression, estimated mean survival was 20.8 months (95% CI, 17.1–24.4); in comparison, mean survival of patients with above-median *NLGN3* expression was 15.2 months (95% CI, 13.1–17.2). On Cox regression analysis, the hazard ratio for death with high versus low *NLGN3* expression was 1.31 (95% CI, 1.05–1.63). *NLGN3* expression was also significantly inversely associated with patient survival in a



continuous Cox proportional-hazards regression analysis, such that higher expression represented an unfavorable prognosis (hazard ratio for death with high versus low *NLGN3* expression, 1.15; 95% CI, 1.01–1.30;  $p < 0.05$ ).

To examine the specificity of these findings, we explored the relationship of neuroligin-2 (*NLGN2*) to survival in human GBM. Recombinant *NLGN2* does not promote pHGG proliferation in vitro (Figure S7D). Likewise, there is no significant association between *NLGN2* expression and patient survival in adult GBM, assessed as above in a continuous Cox model (hazard ratio for death with high versus low *NLGN2* expression, 0.95; 95% CI, 0.78–1.16;  $p = 0.634$ ) and in a two-class model stratified by median expression ( $p = 0.795$  by the log-rank test; Figure S7E).

Interestingly, upon examination of *NLGN3* expression by molecular GBM subtype as defined by TCGA (Verhaak et al., 2010), *NLGN3* expression was significantly lower in the mesenchymal subtype compared to classical, neural, and proneural subtypes (asymptotic significance of  $p < 0.001$  by independent-samples Kruskal-Wallis test; Figure 7B). Notably, *NLGN3* expression remained significantly associated with patient survival in a multivariate Cox model that incorporates molecular subtype (hazard ratio for death with high versus low *NLGN3* expression, 1.15; 95% CI, 1.01–1.30;  $p < 0.05$ ).

**Figure 7. Neuroligin-3 Expression Inversely Correlates with Survival in Human Glioblastoma**

(A) A two-class model stratified by median *NLGN3* expression in 429 GBM cases with molecular subtype data from the TCGA (<http://cancergenome.nih.gov>). Mean overall survival decreases by ~5.6 months in patients with tumors exhibiting above-median *NLGN3* expression;  $p < 0.05$  by the log-rank test.

(B) GBM subtype-specific *NLGN3* expression. Box plots show the smallest and largest observations (top and bottom whiskers, respectively), the interquartile (IQ) range (box), and the median (black line). Data points more than 1.5 times the IQ range lower than the first quartile or 1.5 times the IQ range higher than the third quartile were considered outliers (shown as circles outside the box and whisker plot). Corresponding table of Kruskal-Wallis one-way ANOVAs with  $p$  values indicates pairwise comparisons of *NLGN3* expression in the four subtypes and significance of differential *NLGN3* expressions. See also Figure S7, Table S4.

## DISCUSSION

### Neurons in the Glioma Microenvironment

The results presented here demonstrate that excitatory neuronal activity can influence brain cancer growth. This represents a striking example of the core physiological function of an organ promoting the growth of a cancer arising within it.

An important mechanism mediating this

key microenvironmental interaction is activity-regulated secretion of *NLGN3*. The importance of *NLGN3* in HGG pathophysiology is underscored by the finding that *NLGN3* expression strongly predicts survival in human HGG. Taken together, these data elucidate a fundamental dimension of the HGG microenvironment and identify a robust and targetable mechanism driving HGG proliferation.

The role that neurons may play in brain cancer is underscored by perineuronal satellitosis, the histopathological hallmark of multiple forms of glioma characterized by tumor cell clustering around neuronal somata (Scherer 1938). A wealth of elegant data illustrates that neurotransmitters and neuropeptides can affect glioma cell behavior (Cuddapah et al., 2014; Labrakakis et al., 1998; Seifert and Sontheimer, 2014; Synowitz et al., 2001); for example, glutamate secreted from glioma cells influences their own proliferation and invasion through autocrine/paracrine signaling and subsequently increases the excitability of affected cortical networks (Buckingham et al., 2011; Campbell et al., 2012; Ishiuchi et al., 2002, 2007). However, a direct influence exerted by active parenchymal neurons upon the glioma environment has not been well appreciated. The critical role of neural elements in the cancer microenvironment has recently been elucidated for prostate (Magnon et al., 2013), pancreatic

(Stopczynski et al., 2014) and gastric (Zhao et al., 2014) cancers, in which peripheral innervation was found to potently promote cancer progression. Our results suggest that active neurons play an important role in the microenvironment of brain tumors through malignant hijacking of mechanisms central to brain plasticity.

### Normal and Malignant Neuron-Glial Interactions

A surprisingly broad range of molecularly and clinically distinct classes of HGG exhibited neuronal activity-regulated proliferation, and this response to neuronal activity mirrors that of putative HGG cells of origin. While the cellular origins of HGG may vary among subtypes of the disease, mounting evidence suggests that not only oligodendrogliomas (Persson et al., 2010; Sugiarto et al., 2011), but also many high-grade astroglomas, arise from precursor cells in the oligodendroglial lineage, including NPCs/early OPCs (Monje et al., 2011) and OPCs (Liu et al., 2011; Galvao et al., 2014; Glasgow et al., 2014). OPCs, the most mitotically active cells in the postnatal brain (Geha et al., 2010), may be particularly susceptible to malignant transformation due to Olig2-mediated suppression of p53 function (Mehta et al., 2011). Overexpression of a single transcription factor can determine the oligodendroglial or astrocytic phenotype of oligodendroglial lineage cell-derived tumors (Glasgow et al., 2014). A salient example of this point is the tumor from which the adult GBM culture SU-GBM052 used in this study was derived, a grade IV astrocytoma apparently arising from a transformed grade II oligodendroglioma. The “proneural,” and to a lesser extent the “neural” and “classical,” molecular subtypes of adult GBM, are defined by expression of oligodendroglial lineage-associated genes (Verhaak et al., 2010). Intriguingly, our data demonstrate that *NLGN3* is expressed abundantly in these three subtypes of GBM compared to “mesenchymal” GBM, supporting the concept of a lineage-specific molecular relevance of *NLGN3* to gliomagenesis. Normal NPCs and OPCs respond briskly to neuronal activity, and in the healthy juvenile and adult brain this response results in the activity-regulated generation of mature oligodendrocytes and remodeling of myelin, improving the function of that active circuit (Gibson et al., 2014). The findings presented here suggest that the malignant counterparts of these activity-responsive neural precursor cells may exploit mechanisms of myelin development and plasticity to promote growth.

### Neuroligin-3 in Health and Disease

The finding that *NLGN3* is a glioma mitogen opens numerous doors to a deeper mechanistic understanding of its role in health and disease. The neuroligins are post-synaptic adhesion molecules that are important in synaptic function and plasticity (Südhof, 2008; Varoqueaux et al., 2006). *Nlgn1* and *Nlgn3* are found in excitatory synapses, while *Nlgn2* participates in inhibitory synapses (Gibson et al., 2009; Südhof, 2008). The canonical binding partners of the neuroligins are presynaptic  $\beta$ -neurexins (Ichtchenko et al., 1996; Südhof, 2008). While wild-type neuroligins play a central role in normal synaptic function, *NLGN3* mutations are implicated in altered synaptic function in autism (Jamain et al., 2003; Rothwell et al., 2014; Tabuchi et al., 2007). Our data show that somatic mutations and amplifications in

*NLGN3* are also found at varying frequency in different types of human malignancies, supporting a possibly broader role of *NLGN3* in cancer. Such mutations are less frequent in gliomas, implying that non-genetic mechanisms of *NLGN3* deregulation may predominate in neoplasms of organs that normally express *NLGN3*. Such mechanisms may include, as we show here, activity-regulated secretion coupled with a positive feedforward effect on expression. Interestingly, *NLGN3* mutations and amplifications are prominent in pancreatic, prostate, and gastric cancers, for which a cancer growth-promoting role of innervation has been demonstrated (Stopczynski et al., 2014; Magnon et al., 2013; Zhao et al., 2014).

### Neuroligin Secretion

*Nlgn1* and *Nlgn2* are known to undergo activity-dependent cleavage at the C-terminal transmembrane and cytoplasmic domain with resultant secretion of the N-terminal ectodomain (Peixoto et al., 2012; Suzuki et al., 2012). The data presented here illustrate activity-regulated secretion of *Nlgn3* in the context of cortical projection neuronal activity. The mechanism of *Nlgn3* secretion remains to be seen, but the apparent absence of the C-terminal transmembrane and cytoplasmic domain in the *Nlgn3* protein identified in the active slice CM suggests similarities with mechanisms of *Nlgn1* and *Nlgn2* secretion. Given the enormous complexity of neurexin splice variants (> 1,000; Ullrich et al., 1995) and possible alternative binding partners (Samarelli et al., 2014), the identity of the binding partner for *NLGN3* in glioma cells remains an open question for further exploration.

While the present study provides evidence that active neurons promote HGG proliferation, this intercellular interaction may be indirect. Neuronal activity influences multiple cell types within an active neural circuit, and numerous activity-responsive cell types could play a role in promoting glioma growth. It is possible that *NLGN3* is secreted directly from active neurons or from OPCs, which act as post-synaptic cells in axoglial synapses (Bergles et al., 2010; Bergles et al., 2000) and express the highest level of *Nlgn3* mRNA of any neural cell type (Zhang et al., 2014).

### Neuroligin-3, PI3K Pathway, and Feedforward Expression

How *NLGN3* recruits the glioma cell PI3K pathway is not yet clear, but links between neuroligin binding and receptor tyrosine kinase (RTK) activation, frequently upstream of PI3K, have been described in other contexts. *Nlgn1* binding to *Nrxn1 $\beta$*  in presynaptic neurons promotes neurite outgrowth in a manner that depends upon *Nrxn1 $\beta$* -mediated activation of the RTK fibroblast growth factor receptor-1 (Fgfr1; Gjørland et al., 2012). A similar *NRXN*-RTK interaction may mediate *NLGN3* stimulation of PI3K activity in HGG if a *NRXN* family member is indeed the binding partner of *NLGN3* in glioma cells.

PI3K-mediated feedforward regulation of *NLGN3* gene and protein expression was unexpected. *NLGN3* is not part of the canonical PI3K gene expression signature (Creighton et al., 2010), and, as demonstrated above, other growth factors known to stimulate PI3K such as EGF do not elicit changes in *NLGN3* gene expression in glioma cells, indicating that *NLGN3* is not a general marker of PI3K activity but is rather specific to this context. PI3K has been shown to regulate *Nlgn1* and *Nlgn2*

translation (Gkogkas et al., 2013), suggesting another link between PI3K pathway activity and regulation of *NLGN3* expression. Future work will elucidate the manner in which *NLGN3* recruits PI3K and subsequently promotes feedforward glioma *NLGN3* expression.

### Additional Mechanisms of Neuronal Activity-Regulated Glioma Proliferation

It is also important to note that *NLGN3* is almost certainly not the only important mechanism promoting activity-regulated glioma growth. Indeed, GRP78 and BDNF were also identified as glioma mitogens, and accordingly, *Nlgn3* depletion resulted in a significant but incomplete abrogation of the mitogenic capacity of the CM, indicating partial contributions from other mitogens such as these. Recent single-cell analyses have elucidated intratumoral cellular heterogeneity in HGG (Patel et al., 2014), and it is not yet clear if these different activity-regulated mitogens act on the same or different cellular subpopulations. The candidate activity-dependent mitogens were recognized here via differential regulation and secretion that enabled their identification in the CM following a burst of cortical neuronal activity. Beyond these candidates, additional possible mitogens could be secreted in a more local manner or on a different timescale that precludes their identification within this experimental paradigm. Cell-contact-mediated mechanisms of activity-regulated glioma growth were also not evaluated in our in situ system. One mechanism that we do not evaluate explicitly is activity-regulated glutamate release. Certainly, glutamate released by glioma cells (Buckingham et al., 2011; Campbell et al., 2012; Ishiuchi et al., 2002, 2007) is well-demonstrated to promote glioma growth, and local neuronal glutamate release could function similarly, possibly contributing to the mitogenic effect of active neurons witnessed in vivo.

### Conclusions

*NLGN3* was identified as an unexpected mitogen promoting HGG growth. It is yet unclear whether *NLGN3* similarly mediates healthy myelin plasticity, which future work should address. If that proves to be the case, this important synaptic protein could represent a mechanism of coupling synaptic plasticity and myelin plasticity. Regardless, neuron-glioma cell interactions, including *NLGN3* secretion and subsequent signaling to the oncogenic PI3K-mTOR pathway in glioma cells, represent therapeutic targets for this group of devastating brain tumors.

### EXPERIMENTAL PROCEDURES

See the [Extended Experimental Procedures](#) for detailed experimental procedures.

#### Isolation and Culture of the Primary Human Tumor Cells

Tumor tissue was dissociated and cultured as described in the [Extended Experimental Procedures](#).

#### Orthotopic Xenografting

600,000 SU-pcGBM2 cells were stereotactically implanted into the M2 pre-motor cortex of Thy1::ChR2;NSG or WT;NSG littermate mice at P35. Cells were allowed to engraft for at least 2 months prior to placement of an optical-neural interface for optogenetic stimulation.

#### In Vivo Optogenetic Stimulation

At least 7 days prior to stimulation, the optical-neural interface was placed just below the pial surface of the cortex ipsilateral to xenografts. For the single stimulation paradigm, animals were stimulated with cycles of 473 nm light pulses at 20 Hz for 30 s, followed by 90 s of recovery over a 30 min period and sacrificed 24 hr after stimulation. For the repetitive stimulation paradigm, animals were stimulated as above for 10 min periods on 7 consecutive days and were sacrificed 48 hr after the final session.

#### Generation of Conditioned Media

In short, Thy1::ChR2 or WT mouse brains were cut in 350  $\mu$ m sections on a vibratome, allowed to recover, and stimulated at 20 Hz using a blue-light LED transmitted through the microscope objective. Surrounding medium was then collected for immediate use or frozen at  $-80^{\circ}\text{C}$  for future experiments.

#### Determination of Cell Proliferation In Vitro

To assess the number of cells actively entering S phase in response to various conditions (see [Extended Experimental Procedures](#)), patient-derived glioma cell cultures were exposed to cortical slice CM or various recombinant proteins along with 10  $\mu$ M EdU and were fixed after 24 hr. EdU incorporation was determined using Click-iT EdU visualization (Invitrogen).

#### Proteomic Analysis

Determination of proteins found within the active CM was done using 2D-gel electrophoresis accompanied by LC MS/MS.

#### Western Blot Analysis

Protein levels were determined using western blot analyses. Briefly, after various treatments, 400,000 SU-pcGBM2 cells were lysed and loaded onto SDS-PAGE gels. Proteins were separated with gel electrophoresis and transferred to a PVDF membrane. Proteins were then probed with various antibodies as described in [Extended Experimental Procedures](#).

#### qPCR

After various cell treatments (described in [Extended Experimental Procedures](#)), RNA was extracted from 500,000 SU-pcGBM2 or SU-DIPGXIII cells using TRIzol reagent. cDNA was generated using RT-PCR, and gene expression changes were further probed using quantitative PCR.

### ACCESSION NUMBERS

The accession number for RNA-seq data deposited in the GEO database is GEO: GSE62563.

### SUPPLEMENTAL INFORMATION

Supplemental Information includes [Extended Experimental Procedures](#), seven figures, one movie, and four tables and can be found with this article online at <http://dx.doi.org/10.1016/j.cell.2015.04.012>.

### AUTHOR CONTRIBUTIONS

H.S.V. and T.B.J. conducted all experiments and contributed to experimental design, manuscript editing, and data analysis for all sections. V.C. contributed to conducting in vivo experiments and to experimental design. M.M. designed all experiments, wrote the manuscript, and supervised all aspects of the work.

### ACKNOWLEDGMENTS

The authors gratefully acknowledge support from the Matthew Larson Foundation, Godfrey Family Fund in Memory of Fiona Penelope, National Institute of Neurological Disorders and Stroke (NINDS K08NS070926), McKenna Claire Foundation, National Science Foundation Graduate Research Fellowship Program, California Institute for Regenerative Medicine (CIRM RB4-06093 and RN3-06510), Alex's Lemonade Stand Foundation, The Cure Starts Now

Foundation, Lyla Nsouli Foundation, Unravel Pediatric Cancer, the Wayland Villars DIPG Foundation, the Dylan Jewett, Connor Johnson, Zoey Ganesh, Dylan Frick, Abigail Jensen, and Jennifer Kranz Memorial Funds, Virginia and D.K. Ludwig Fund for Cancer Research, the Bear Necessities Pediatric Cancer Foundation, Lucile Packard Foundation for Children's Health, Stanford University School of Medicine Dean's Fellowship, Child Health Research Institute at Stanford Anne T. and Robert M. Bass Endowed Faculty Scholarship in Pediatric Cancer and Blood Diseases, National Cancer Institute (PSOC-MCSTART U54CA143907), Canary Foundation, Ben and Catherine Ivy Foundation, and the Sujal and Meera Patel Foundation. Special thanks to Sarah Chen for illustrations, to Elizabeth Hoyte for assistance with figures, to Eric Raabe for use of the JHH-DIPGI cell line, and to Tom Südhof for helpful discussions.

Received: October 17, 2014

Revised: January 24, 2015

Accepted: March 3, 2015

Published: April 23, 2015

## REFERENCES

- Arenkiel, B.R., Peca, J., Davison, I.G., Feliciano, C., Deisseroth, K., Augustine, G.J., Ehlers, M.D., and Feng, G. (2007). In vivo light-induced activation of neural circuitry in transgenic mice expressing channelrhodopsin-2. *Neuron* 54, 205–218.
- Bergles, D.E., Roberts, J.D., Somogyi, P., and Jahr, C.E. (2000). Glutamatergic synapses on oligodendrocyte precursor cells in the hippocampus. *Nature* 405, 187–191.
- Bergles, D.E., Jabs, R., and Steinhäuser, C. (2010). Neuron-glia synapses in the brain. *Brain Res. Brain Res. Rev.* 63, 130–137.
- Boyden, E.S., Zhang, F., Bamberg, E., Nagel, G., and Deisseroth, K. (2005). Millisecond-timescale, genetically targeted optical control of neural activity. *Nat. Neurosci.* 8, 1263–1268.
- Buckingham, S.C., Campbell, S.L., Haas, B.R., Montana, V., Robel, S., Ogunrinu, T., and Sontheimer, H. (2011). Glutamate release by primary brain tumors induces epileptic activity. *Nat. Med.* 17, 1269–1274.
- Campbell, S.L., Buckingham, S.C., and Sontheimer, H. (2012). Human glioma cells induce hyperexcitability in cortical networks. *Epilepsia* 53, 1360–1370.
- Charles, N.A., Holland, E.C., Gilbertson, R., Glass, R., and Kettenmann, H. (2011). The brain tumor microenvironment. *Glia* 59, 1169–1180.
- Chen, D.B., and Davis, J.S. (2003). Epidermal growth factor induces c-fos and c-jun mRNA via Raf-1/MEK1/ERK-dependent and -independent pathways in bovine luteal cells. *Mol. Cell. Endocrinol.* 200, 141–154.
- Creighton, C.J., Fu, X., Hennessy, B.T., Casa, A.J., Zhang, Y., Gonzalez-Angulo, A.M., Lluch, A., Gray, J.W., Brown, P.H., Hilsenbeck, S.G., et al. (2010). Proteomic and transcriptomic profiling reveals a link between the PI3K pathway and lower estrogen-receptor (ER) levels and activity in ER+ breast cancer. *Breast Cancer Res.* 12, R40.
- Cuddapah, V.A., Robel, S., Watkins, S., and Sontheimer, H. (2014). A neurocentric perspective on glioma invasion. *Nat. Rev. Neurosci.* 15, 455–465.
- Fan, Q.W., Cheng, C., Knight, Z.A., Haas-Kogan, D., Stokoe, D., James, C.D., McCormick, F., Shokat, K.M., and Weiss, W.A. (2009). EGFR signals to mTOR through PKC and independently of Akt in glioma. *Sci. Signal.* 2, ra4.
- Galvao, R.P., Kasina, A., McNeill, R.S., Harbin, J.E., Foreman, O., Verhaak, R.G., Nishiyama, A., Miller, C.R., and Zong, H. (2014). Transformation of quiescent adult oligodendrocyte precursor cells into malignant glioma through a multistep reactivation process. *Proc. Natl. Acad. Sci. USA* 111, E4214–E4223.
- Geha, S., Pallud, J., Junier, M.P., Devaux, B., Leonard, N., Chassoux, F., Chneiweiss, H., Daumas-Duport, C., and Varlet, P. (2010). NG2+/Olig2+ cells are the major cycle-related cell population of the adult human normal brain. *Brain Pathol.* 20, 399–411.
- Gerlee, P. (2013). The model muddle: in search of tumor growth laws. *Cancer Res.* 73, 2407–2411.
- Gibson, J.R., Huber, K.M., and Südhof, T.C. (2009). Neuroligin-2 deletion selectively decreases inhibitory synaptic transmission originating from fast-spiking but not from somatostatin-positive interneurons. *J. Neurosci.* 29, 13883–13897.
- Gibson, E.M., Purger, D., Mount, C.W., Goldstein, A.K., Lin, G.L., Wood, L.S., Inema, I., Miller, S.E., Bieri, G., Zuchero, J.B., et al. (2014). Neuronal activity promotes oligodendrogenesis and adaptive myelination in the mammalian brain. *Science* 344, 1252304.
- Gjorlund, M.D., Nielsen, J., Pankratova, S., Li, S., Korshunova, I., Bock, E., and Berezin, V. (2012). Neuroligin-1 induces neurite outgrowth through interaction with neuroligin-1β and activation of fibroblast growth factor receptor-1. *FASEB J.* 26, 4174–4186.
- Gkogkas, C.G., Khoutorsky, A., Ran, I., Rampakakis, E., Nevarko, T., Weatherill, D.B., Vasuta, C., Yee, S., Truitt, M., Dallaire, P., et al. (2013). Autism-related deficits via dysregulated eIF4E-dependent translational control. *Nature* 493, 371–377.
- Glasgow, S.M., Zhu, W., Stolt, C.C., Huang, T.W., Chen, F., LoTurco, J.J., Neul, J.L., Wegner, M., Mohila, C., and Deneen, B. (2014). Mutual antagonism between Sox10 and NFIA regulates diversification of glial lineages and glioma subtypes. *Nat. Neurosci.* 17, 1322–1329.
- Gonzales, M., and Bowden, G.T. (2002). The role of PI 3-kinase in the UVB-induced expression of c-fos. *Oncogene* 21, 2721–2728.
- Greenberg, M.E., and Ziff, E.B. (1984). Stimulation of 3T3 cells induces transcription of the c-fos proto-oncogene. *Nature* 311, 433–438.
- Ichtchenko, K., Nguyen, T., and Südhof, T.C. (1996). Structures, alternative splicing, and neuroligin binding of multiple neuroligins. *J. Biol. Chem.* 271, 2676–2682.
- Ishiyuchi, S., Tsuzuki, K., Yoshida, Y., Yamada, N., Hagimura, N., Okado, H., Miwa, A., Kurihara, H., Nakazato, Y., Tamura, M., et al. (2002). Blockage of Ca<sup>2+</sup>-permeable AMPA receptors suppresses migration and induces apoptosis in human glioblastoma cells. *Nat. Med.* 8, 971–978.
- Ishiyuchi, S., Yoshida, Y., Sugawara, K., Aihara, M., Ohtani, T., Watanabe, T., Saito, N., Tsuzuki, K., Okado, H., Miwa, A., et al. (2007). Ca<sup>2+</sup>-permeable AMPA receptors regulate growth of human glioblastoma via Akt activation. *J. Neurosci.* 27, 7987–8001.
- Jamain, S., Quach, H., Betancur, C., Råstam, M., Colineaux, C., Gillberg, I.C., Soderstrom, H., Giros, B., Leboyer, M., Gillberg, C., and Bourgeron, T.; Paris Autism Research International Sibpair Study (2003). Mutations of the X-linked genes encoding neuroligins NLGN3 and NLGN4 are associated with autism. *Nat. Genet.* 34, 27–29.
- Johannessen, A.L., and Torp, S.H. (2006). The clinical value of Ki-67/MIB-1 labeling index in human astrocytomas. *Pathol. Oncol. Res.* 12, 143–147.
- Khuong-Quang, D.A., Buczkowicz, P., Rakopoulos, P., Liu, X.Y., Fontebasso, A.M., Bouffet, E., Bartels, U., Albrecht, S., Schwartzentruber, J., Letourneau, L., et al. (2012). K27M mutation in histone H3.3 defines clinically and biologically distinct subgroups of pediatric diffuse intrinsic pontine gliomas. *Acta Neuropathol.* 124, 439–447.
- Labrakakis, C., Patt, S., Hartmann, J., and Kettenmann, H. (1998). Functional GABA(A) receptors on human glioma cells. *Eur. J. Neurosci.* 10, 231–238.
- Lee, H.K., Xiang, C., Cazacu, S., Finniss, S., Kazimirsky, G., Lemke, N., Lehman, N.L., Rempel, S.A., Mikkelsen, T., and Brodie, C. (2008). GRP78 is overexpressed in glioblastomas and regulates glioma cell growth and apoptosis. *Neuro-oncol.* 10, 236–243.
- Liu, C., Sage, J.C., Miller, M.R., Verhaak, R.G., Hippenmeyer, S., Vogel, H., Foreman, O., Bronson, R.T., Nishiyama, A., Luo, L., and Zong, H. (2011). Mosaic analysis with double markers reveals tumor cell of origin in glioma. *Cell* 146, 209–221.
- Magnon, C., Hall, S.J., Lin, J., Xue, X., Gerber, L., Freedland, S.J., and Frenette, P.S. (2013). Autonomic nerve development contributes to prostate cancer progression. *Science* 341, 1236361.
- Mehta, S., Huillard, E., Kesari, S., Maire, C.L., Golebiowski, D., Harrington, E.P., Alberta, J.A., Kane, M.F., Theisen, M., Ligon, K.L., et al. (2011). The central nervous system-restricted transcription factor Olig2 opposes p53

- responses to genotoxic damage in neural progenitors and malignant glioma. *Cancer Cell* 19, 359–371.
- Monje, M., Mitra, S.S., Freret, M.E., Raveh, T.B., Kim, J., Masek, M., Attena, J.L., Li, G., Haddix, T., Edwards, M.S., et al. (2011). Hedgehog-responsive candidate cell of origin for diffuse intrinsic pontine glioma. *Proc. Natl. Acad. Sci. USA* 108, 4453–4458.
- Patel, A.P., Tirosh, I., Trombetta, J.J., Shalek, A.K., Gillespie, S.M., Wakimoto, H., Cahill, D.P., Nahed, B.V., Curry, W.T., Martuza, R.L., et al. (2014). Single-cell RNA-seq highlights intratumoral heterogeneity in primary glioblastoma. *Science* 344, 1396–1401.
- Peixoto, R.T., Kunz, P.A., Kwon, H., Mabb, A.M., Sabatini, B.L., Philpot, B.D., and Ehlers, M.D. (2012). Transsynaptic signaling by activity-dependent cleavage of neuroligin-1. *Neuron* 76, 396–409.
- Persson, A.I., Petritsch, C., Swartling, F.J., Itsara, M., Sim, F.J., Auvergne, R., Goldenberg, D.D., Vandenberg, S.R., Nguyen, K.N., Yakovenko, S., et al. (2010). Non-stem cell origin for oligodendroglioma. *Cancer Cell* 18, 669–682.
- Pyonteck, S.M., Akkari, L., Schuhmacher, A.J., Bowman, R.L., Sevenich, L., Quail, D.F., Olson, O.C., Quick, M.L., Huse, J.T., Teijeiro, V., et al. (2013). CSF-1R inhibition alters macrophage polarization and blocks glioma progression. *Nat. Med.* 19, 1264–1272.
- Rothstein, J.D., Dykes-Hoberg, M., Pardo, C.A., Bristol, L.A., Jin, L., Kuncl, R.W., Kanai, Y., Hediger, M.A., Wang, Y., Schielke, J.P., and Welty, D.F. (1996). Knockout of glutamate transporters reveals a major role for astroglial transport in excitotoxicity and clearance of glutamate. *Neuron* 16, 675–686.
- Rothwell, P.E., Fuccillo, M.V., Maxeiner, S., Hayton, S.J., Gokce, O., Lim, B.K., Fowler, S.C., Malenka, R.C., and Südhof, T.C. (2014). Autism-associated neuroligin-3 mutations commonly impair striatal circuits to boost repetitive behaviors. *Cell* 158, 198–212.
- Samarelli, A.V., Riccitelli, E., Bizzozero, L., Silveira, T.N., Seano, G., Pergolizzi, M., Vitagliano, G., Cascone, I., Carpentier, G., Bottos, A., et al. (2014). Neuroligin 1 induces blood vessel maturation by cooperating with the  $\alpha 6$  integrin. *J. Biol. Chem.* 289, 19466–19476.
- Scherer, H.J. (1938). Structural development in gliomas. *Am. J. Cancer* 34, 333–351.
- Schwartzentruber, J., Korshunov, A., Liu, X.Y., Jones, D.T., Pfaff, E., Jacob, K., Sturm, D., Fontebasso, A.M., Quang, D.A., Tönjes, M., et al. (2012). Driver mutations in histone H3.3 and chromatin remodelling genes in paediatric glioblastoma. *Nature* 482, 226–231.
- Seifert, S., and Sontheimer, H. (2014). Bradykinin enhances invasion of malignant glioma into the brain parenchyma by inducing cells to undergo amoeboid migration. *J. Physiol.* 592, 5109–5127.
- Silver, D.J., Siebzehnubel, F.A., Schildts, M.J., Yachnis, A.T., Smith, G.M., Smith, A.A., Scheffler, B., Reynolds, B.A., Silver, J., and Steindler, D.A. (2013). Chondroitin sulfate proteoglycans potently inhibit invasion and serve as a central organizer of the brain tumor microenvironment. *J. Neurosci.* 33, 15603–15617.
- Stopczynski, R.E., Normolle, D.P., Hartman, D.J., Ying, H., DeBerry, J.J., Bielefeldt, K., Rhim, A.D., DePinho, R.A., Albers, K.M., and Davis, B.M. (2014). Neuroplastic changes occur early in the development of pancreatic ductal adenocarcinoma. *Cancer Res.* 74, 1718–1727.
- Sturm, D., Witt, H., Hovestadt, V., Khuong-Quang, D.A., Jones, D.T., Konermann, C., Pfaff, E., Tönjes, M., Sill, M., Bender, S., et al. (2012). Hotspot mutations in H3F3A and IDH1 define distinct epigenetic and biological subgroups of glioblastoma. *Cancer Cell* 22, 425–437.
- Südhof, T.C. (2008). Neuroligins and neuexins link synaptic function to cognitive disease. *Nature* 455, 903–911.
- Sugiarto, S., Persson, A.I., Munoz, E.G., Waldhuber, M., Lamagna, C., Andor, N., Hanecker, P., Ayers-Ringler, J., Phillips, J., Siu, J., et al. (2011). Asymmetry-defective oligodendrocyte progenitors are glioma precursors. *Cancer Cell* 20, 328–340.
- Suzuki, K., Hayashi, Y., Nakahara, S., Kumazaki, H., Prox, J., Horiuchi, K., Zeng, M., Tanimura, S., Nishiyama, Y., Osawa, S., et al. (2012). Activity-dependent proteolytic cleavage of neuroligin-1. *Neuron* 76, 410–422.
- Synowitz, M., Ahmann, P., Matyash, M., Kuhn, S.A., Hofmann, B., Zimmer, C., Kirchhoff, F., Kiwit, J.C., and Kettenmann, H. (2001). GABA(A)-receptor expression in glioma cells is triggered by contact with neuronal cells. *Eur. J. Neurosci.* 14, 1294–1302.
- Tabuchi, K., Blundell, J., Etherton, M.R., Hammer, R.E., Liu, X., Powell, C.M., and Südhof, T.C. (2007). A neuroligin-3 mutation implicated in autism increases inhibitory synaptic transmission in mice. *Science* 318, 71–76.
- Ullrich, B., Ushkaryov, Y.A., and Südhof, T.C. (1995). Cartography of neuexins: more than 1000 isoforms generated by alternative splicing and expressed in distinct subsets of neurons. *Neuron* 14, 497–507.
- Varoqueaux, F., Aramuni, G., Rawson, R.L., Mohrmann, R., Missler, M., Gottmann, K., Zhang, W., Südhof, T.C., and Brose, N. (2006). Neuroligins determine synapse maturation and function. *Neuron* 51, 741–754.
- Verhaak, R.G., Hoadley, K.A., Purdom, E., Wang, V., Qi, Y., Wilkerson, M.D., Miller, C.R., Ding, L., Golub, T., Mesirov, J.P., et al.; Cancer Genome Atlas Research Network (2010). Integrated genomic analysis identifies clinically relevant subtypes of glioblastoma characterized by abnormalities in PDGFRA, IDH1, EGFR, and NF1. *Cancer Cell* 17, 98–110.
- Wang, H., Peca, J., Matsuzaki, M., Matsuzaki, K., Noguchi, J., Qiu, L., Wang, D., Zhang, F., Boyden, E., Deisseroth, K., et al. (2007). High-speed mapping of synaptic connectivity using photostimulation in Channelrhodopsin-2 transgenic mice. *Proc. Natl. Acad. Sci. USA* 104, 8143–8148.
- Wang, Y., Yang, J., Zheng, H., Tomasek, G.J., Zhang, P., McKeever, P.E., Lee, E.Y., and Zhu, Y. (2009). Expression of mutant p53 proteins implicates a lineage relationship between neural stem cells and malignant astrocytic glioma in a murine model. *Cancer Cell* 15, 514–526.
- Wu, G., Broniscer, A., McEachron, T.A., Lu, C., Paugh, B.S., Becksfors, J., Qu, C., Ding, L., Huether, R., Parker, M., et al.; St. Jude Children’s Research Hospital–Washington University Pediatric Cancer Genome Project (2012). Somatic histone H3 alterations in pediatric diffuse intrinsic pontine gliomas and non-brainstem glioblastomas. *Nat. Genet.* 44, 251–253.
- Yizhar, O., Fenno, L.E., Davidson, T.J., Mogri, M., and Deisseroth, K. (2011). Optogenetics in neural systems. *Neuron* 71, 9–34.
- Zhang, Y., Chen, K., Sloan, S.A., Bennett, M.L., Scholze, A.R., O’Keefe, S., Phatnani, H.P., Guarnieri, P., Caneda, C., Ruderisch, N., et al. (2014). An RNA-sequencing transcriptome and splicing database of glia, neurons, and vascular cells of the cerebral cortex. *J. Neurosci.* 34, 11929–11947.
- Zhao, C.M., Hayakawa, Y., Kodama, Y., Muthupalani, S., Westphalen, C.B., Anderson, G.T., Flatberg, A., Johannessen, H., Friedman, R.A., Renz, B.W., et al. (2014). Denervation suppresses gastric tumorigenesis. *Sci. Transl. Med.* 6, 250ra115.

## EXTENDED EXPERIMENTAL PROCEDURES

### Mice and Housing Conditions

All in vivo experiments were approved by the Stanford University Institutional Animal Care and Use Committee and performed in accordance with institutional guidelines. Thy1::ChR2 mice (line 20; The Jackson Laboratory, Bar Harbor, ME) were first intercrossed with NSG mice (NOD-SCID-IL2R gamma chain-deficient, The Jackson Laboratory, Bar Harbor, ME) to produce the Thy1::ChR2;NSG genotype. All experiments were performed either on animals heterozygous for Thy1::ChR2 or on WT control NSG littermates. Animals were housed according to standard guidelines with free access to food and water in a 12 hr light/dark cycle.

### Cell Culture

For all human tissue studies, informed consent was obtained and Institutional Review Board (IRB) approval was granted. For all cultures, authenticity is verified and monitored using short tandem repeat (STR) DNA fingerprinting every three months.

Pediatric cortical high-grade glioma culture was generated as follows: Tissue from a pediatric cortical high-grade glioma (WHO grade IV) tumor was obtained at the time of initial biopsy from a 15-year-old male patient under sterile conditions. The tissue was dissociated mechanically, followed by gentle enzymatic dissociation with TrypLE (5 min at 37°C; Life Technologies, Carlsbad, CA) and then passed through a 100- $\mu$ m filter. The flow-through was collected and cultured in a T75cm<sup>2</sup> flask. The filter was inverted and the tissue was flushed and cultured into a separate flask. A defined, serum-free medium designated "Tumor Stem Media (TSM)" was used throughout, consisting of Neurobasal(-A) (Invitrogen, Carlsbad, CA), B27(-A) (Invitrogen, Carlsbad, CA), human-bFGF (20 ng/mL) (Shenandoah Biotech, Warwick, PA), human-EGF (20 ng/mL) (Shenandoah, Biotech, Warwick, PA), human PDGF-AA (10 ng/mL) and PDGF-BB (10 ng/mL) (Shenandoah, Biotech, Warwick, PA) and heparin (2 ng/mL) (Stem Cell Technologies, Vancouver, BC, Canada). When neurospheres were visible in the primary culture it was passed through a 40- $\mu$ m filter to remove debris and single cells such as red blood cells; the matter that did not pass through the filter, containing the larger than 40- $\mu$ m neurospheres, was recovered and subsequently dissociated using TrypLE. A second filtration was then performed using 40- $\mu$ m filters, the single cells in the flow-through were centrifuged at 300 g for 5 min, and the pellet was resuspended in TSM and recultured, generating secondary neurospheres. This cell line was designated SU-pcGBM2 (Stanford University, pediatric cortical glioblastoma line 2), grown in nonadherent neurosphere culture in the above medium, and passaged every one to two weeks.

Diffuse intrinsic pontine glioma (DIPG) tumor neurosphere cultures SU-DIPGIV and SU-DIPGVI were generated as previously described (Caretti et al., 2014; Monje et al., 2011) from early post-mortem tissue donations and grown as tumor neurospheres in defined, serum-free TSM medium as above. SU-DIPGXIII was generated similarly, but using the mechanical dissociation protocol described above. JHH-DIPGI cells, a kind gift from Dr. Eric Raabe at Johns Hopkins Hospital, were generated similarly to the Stanford cultures as neurospheres from post-mortem tissue and are grown under the same media conditions.

The adult high-grade gliomas (WHO grade IV) used were obtained at the time of biopsy and cultured as described previously for DIPG tissue (Monje et al., 2011) but using the mechanical dissociation protocol described above and without PDGF-AA or BB supplementation.

The oligodendroglioma culture was obtained at the time of biopsy. The tumor specimen was chopped into fine pieces with a sterile razor blade, and dissociated enzymatically by incubating in Liberase DH (Roche Life Science, Indianapolis, IN) on a rotator at 37°C for 30 min. Tissue was then passed through a 10 ml serological pipette 8 times, followed by 8 passages through a 1 ml pipette tip. The resulting cell suspension was strained through a 100- $\mu$ m cell strainer to remove large debris, and the flow-through was pelleted and myelin removed by centrifugation in 30% sucrose solution at 800 g. Red blood cells in the resulting pellet were removed by treatment with ACK lysis solution (Life Technologies, Carlsbad, CA), and the remaining cells were plated in culture flasks pre-coated with Matrigel (BD Biosciences, San Jose, CA) in TSM media.

### Orthotopic Xenografting

A single-cell suspension from cultured SU-pcGBM2 neurospheres at passage 19-22 was prepared in sterile PBS immediately prior to the xenograft procedure. Animals at P34-36 were anesthetized with 1%–4% isoflurane and placed in a stereotactic apparatus. The cranium was exposed via midline incision under aseptic conditions. 600,000 SU-pcGBM2 cells in 3  $\mu$ l sterile PBS were stereotactically implanted in the premotor cortex (M2) of the right hemisphere through a 31-gauge burr hole, using a digital pump at infusion rate of 0.4  $\mu$ L/min and 31-gauge Hamilton syringe. Stereotactic coordinates used were as follows: 0.5 mm lateral to midline, 1.0 mm anterior to bregma, –1.75 mm deep to cranial surface. At the completion of infusion, syringe needle was allowed to remain in place for a minimum of 2 min, then manually withdrawn at a rate of 0.875 mm/min to minimize backflow of the injected cell suspension.

### Fiber Optic Placement and In Vivo Optogenetic Stimulation

Fiber optic placement was performed as previously described (Gibson et al., 2014) a minimum of 7 days prior to optogenetic stimulation. Animals were anesthetized with 1%–4% isoflurane and placed in a stereotactic apparatus. The cranium was exposed using a midline incision under aseptic conditions. A fiber optic ferrule (Doric Lenses, Quebec, Canada) was placed at the premotor cortex (M2) of the right hemisphere using the following coordinates: 0.5 mm lateral to midline, 1.0 mm anterior to bregma, –0.6 mm deep to cranial surface in the right hemisphere. At 10-11 weeks post-xenograft (allowing a minimum of 7 days of recovery following

ferrule placement procedure), all animals were connected to a 100-mW 473-nm DPSS laser system with a mono fiber patch cord, which freely permits wakeful behavior of the animal. Pulses of light with  $\sim 10$  mW measured output at tip of the patch cord were administered at a frequency of 20 Hz for periods of 30 s, followed by 90 s recovery periods, for a total session duration of 30 min for single-session stimulation paradigms or 10 min per day for 7 consecutive days for the repetitive stimulation paradigm. This power represents  $\sim 30$  mW/cm<sup>2</sup> light density at the tip of the patch cord; with the optical ferrule placed just below the pial surface this would deliver  $\sim 3$  mW/cm<sup>2</sup> approximately midway through the cortex to reach the layer V apical dendrites (Yizhar et al., 2011). This was the minimum light required to reliably elicit complex motor behavioral output. This paradigm is modified slightly from that previously described (Gibson et al., 2014), with a 90 s recovery period rather than 120 s and higher light density required to elicit the complex motor behavior in tumor-bearing NSG mice rather than non-tumor-bearing mice with a CD1/B6 mixed background. When tumor-bearing Thy1::ChR2;NSG animals are stimulated in parallel with non-tumor bearing Thy1::ChR2 animals on a mixed CD1/B6 background, the tumor-bearing NSG background mice consistently required higher light power to elicit the expected motor behavior (unidirectional ambulation). During periods of light administration, all Thy1::ChR2;NSG animals responded with unidirectional ambulation to the left for the duration of light exposure (Movie S1), confirming proper ferrule placement over right M2 and effective neuronal stimulation. All WT;NSG animals demonstrated no change in behavioral output in response to light stimulation. Following stimulation in the single-session paradigm, an intraperitoneal injection of 5-ethynyl-2'-deoxyuridine (EdU; 40 mg/kg; Invitrogen, Carlsbad, CA) was administered to the animal. Mice were sacrificed 24 hr after administration of EdU in the single-session paradigm experiment. For the repetitive stimulation experiment, mice were sacrificed 48 hr following the final (7<sup>th</sup>) stimulation session.

### Perfusion and Immunohistochemistry

Animals were anesthetized with intraperitoneal Avertin (tribromoethanol), then transcardially perfused with 20 ml of PBS. Brains were fixed in 4% paraformaldehyde overnight at 4°C, then transferred to 30% sucrose for cryoprotection. Brains were embedded in Tissue-Tek O.C.T. (Sakura, Torrance, CA) and sectioned in the coronal plane at 40  $\mu$ m using a sliding microtome (Microm HM450; Thermo Scientific, Waltham, MA). For immunohistochemistry, a 1 in 6 series of 40- $\mu$ m coronal sections was stained using the Click-iT EdU cell proliferation kit and protocol (Life Technologies, Carlsbad, CA) to expose EdU labeling, then incubated in blocking solution (3% normal donkey serum, 0.3% Triton X-100 in TBS) at room temperature for 30 min. Mouse anti-human nuclei clone 235-1 (1:100; Millipore, Billerica, MA), rabbit anti-Ki67 (1:500; Abcam, Cambridge, MA), rat anti-MBP (1:200; Abcam, Cambridge, MA) and rabbit anti-cleaved caspase-3 (1:200; Cell Signaling, Danvers, MA) were diluted in 1% blocking solution (1% normal donkey serum in 0.3% Triton X-100 in TBS) and incubated overnight at 4°C. Sections were then rinsed three times in 1X TBS and incubated in secondary antibody solution (Alexa 488 goat anti-mouse IgG, 1:500 (Life Technologies, Carlsbad, CA); Alexa 488 donkey anti-rabbit IgG, 1:500 (Life Technologies, Carlsbad, CA); Alexa 594 donkey anti-mouse IgG, 1:500 (Life Technologies, Carlsbad, CA); Alexa 647 donkey anti-rabbit IgG, 1:500 (Life Technologies, Carlsbad, CA); Alexa 594 donkey anti-rat IgG, 1:1000 (Life Technologies, Carlsbad, CA)) in 1% blocking solution at 4°C overnight. The next day, sections were rinsed 3 times in TBS and mounted with ProLong Gold mounting medium with DAPI (Life Technologies, Carlsbad, CA).

### Confocal Imaging and Quantification

#### Analysis of Cell Proliferation and Cell Death

Cell quantification was performed by live counting at 400x magnification using a Zeiss LSM700 scanning confocal microscope and Zen 2011 imaging software (Carl Zeiss Inc., Pleasanton, CA). For the single-session stimulation paradigm, the area for quantification within the active circuit was selected as follows: of a 1 in 6 series of 40- $\mu$ m coronal sections, 3 consecutive sections were selected at approximately 1.1–0.86 mm anterior to bregma (Figures 22, 23, 24 in Paxinos and Franklin, 2008); using our stereotactic coordinates for tumor xenograft, these sections are expected to include the tissue most proximal to the site of tumor cell implantation in the coronal plane. For each of the three consecutive sections, the cingulum bundle was first identified as an anatomic landmark, and a 160x160- $\mu$ m field area for quantification (Figure S1C, Field 1) was selected immediately superficial to this landmark within cortical layer 6b of M2. A second field (Field 2) was selected immediately deep to this landmark in the corpus callosum. Two additional quantification fields (3,4) were selected so as to lie within cortical layer 6b/6a, immediately superficial to the topmost edge of Field 1, and juxtaposed side-by-side about the Field 1 mediolateral midpoint. Similarly, two additional quantification fields (5,6) were selected so as to lie within the corpus callosum, immediately deep to the bottommost edge of Field 2, and juxtaposed side-by-side about the Field 2 mediolateral midpoint (see schematic Figure S1C). As each field was live-counted through the entire slice thickness of 40  $\mu$ m, the total volume quantified per field was  $1.024 \times 10^6 \mu\text{m}^3$ ; six fields within each of three coronal sections were selected for a total quantified volume of  $18.432 \times 10^6 \mu\text{m}^3$  per animal. These selected premotor cortex and corpus callosum areas lie within the active premotor circuit, but are deep to the path of tumor cell injection by our stereotactic coordinates, and thus avoid the principal areas of inflammatory change involving tissue more proximal to the injection site. Within each field, all human nuclear antigen (HNA)-positive tumor cells were quantified to determine tumor burden within the areas quantified. HNA-positive tumor cells were then assessed for double-labeling with either EdU or Ki67 (cell proliferation), or with cleaved caspase-3 (cell death). To calculate proliferation index (the percentage of proliferating tumor cells for each animal), the total number of HNA-positive cells co-labeled with EdU across all areas quantified was divided by the total number of human nuclei-positive cells counted across all areas quantified. This was repeated for human nuclei-positive cells assessed for double-labeling with Ki67 (proliferation index) or for cleaved caspase-3

(cell death). For cleaved caspase-3 staining, ischemic mouse brain tissue was used as a positive staining control (brain placed in PBS after removal at 37°C for five hours prior to fixation with 4% paraformaldehyde overnight, then transferred to 30% sucrose for cryoprotection).

Using the same selected coronal tissue sections of the 1 in 6 series, the area of quantification outside the active circuit was selected as follows: for each of the three consecutive sections per animal, the cingulum bundle was first identified as an anatomic landmark, and a 160x160- $\mu\text{m}$  field area for quantification was selected in the prefrontal cortex adjacent to the longitudinal fissure and medial to the cingulum bundle. Two additional fields were selected side-by-side moving laterally in the prefrontal cortex but outside the active circuit, for a total quantified volume of  $9.216 \times 10^6 \mu\text{m}^3$  per animal (Figure S1D).

#### **Analysis of Tumor Cell Burden**

Animals were included that had well-matched xenografts with respect to location of injection tract in the rostro-caudal dimension and with respect to cortical depth. The target location was midway through the cortical depth and just outside of the rostro-caudal center of premotor area M2 but within  $\sim 240 \mu\text{m}$  of the premotor area M2 midpoint in the rostro-caudal dimension; in this way, the xenografted cells diffusely infiltrate the area of optogenetic stimulation in M2 but xenograft needle injury and optical ferrule placement are not induced in the same coronal plane. For the repetitive stimulation experiment, two litters of mice born one day apart were xenografted two days apart at  $\sim$ P35 using two separate flasks of SU-pcGBM2 cells (at passage 19 and passage 20, respectively). The two litters had optical-neural interfaces placed as above at 9 weeks following xenotransplantation and were stimulated at 10 weeks following xenotransplantation in parallel. Because these two litters were xenografted on different days with cells from different flasks, the data were normalized to the mean tumor cell density of the identically manipulated WT control animals from each litter. Tumor cell burden was analyzed in the superior  $\sim 1/3$  of the corpus callosum, 100  $\mu\text{m}$  deep to the cortical-corporum callosum border, the region containing the most dense projections from both M2 and M1 motor cortices (Allen Brain Atlas). Quantification of HNA-positive cell density was performed by a blinded investigator as follows: three consecutive sections of a 1 in 2 series of 40- $\mu\text{m}$  coronal sections were selected for closest proximity to the site of fiber optic placement. For each section, a maximum-intensity projection image of a z-stack of 6 slices 6  $\mu\text{m}$  apart through the thickness of the section was obtained at 100x magnification using a Zeiss LSM700 scanning confocal microscope and Zen 2011 imaging software (Carl Zeiss, Pleasanton, CA). HNA-positive tumor cells were then counted within five 100  $\mu\text{m}$  x 100  $\mu\text{m}$  boxed counting areas aligned with the cortical-corporum callosum border and centered about the apex of the cingulum bundle in the maximum intensity projection images using Adobe Photoshop software (Adobe, San Jose, CA).

#### **Electrophysiology in Slices**

Coronal brain sections containing the motor cortex were cut from Thy1::ChR2 mice. Following isoflurane anesthesia, animals were decapitated and the brain rapidly removed and placed in ice-cold, oxygenated artificial CSF (aCSF) containing (in mM): 118 NaCl, 2.5 KCl, 2.5 NaHCO<sub>3</sub>, 10 glucose, 1.3 MgCl<sub>2</sub>, 2.5 CaCl<sub>2</sub>, and 1.2 NaH<sub>2</sub>PO<sub>4</sub>. Slices were cut in 300  $\mu\text{m}$  sections using a vibratome (Leica VT 1200S, Buffalo Grove, IL), and incubated at 32°C for 30 min before being allowed to equilibrate at room temperature for at least a further 30 min. During recording, slices were perfused with heated aCSF ( $32 \pm 2^\circ\text{C}$ ). For whole cell current clamp recordings from Layer V/VI motor cortical pyramidal cells, recording pipettes (3-5 M $\Omega$ ) fabricated from borosilicate glass were filled with a solution containing (in mM): 135 KMeSO<sub>4</sub>, 8 NaCl, 10 HEPES, 2 Mg<sub>2</sub>ATP, 0.3 Na<sub>3</sub>GTP, 0.1 spermine, 7 phosphocreatine, and 0.3 EGTA. GABA<sub>A</sub> antagonist picrotoxin (100  $\mu\text{M}$ ) and AMPA receptor antagonist NBQX (10  $\mu\text{M}$ ) were added to the aCSF during all the experiments. 25-ms light pulses were delivered at 20 Hz for 15 min to evoke ChR2-mediated action potentials. All recordings were made using MultiClamp 700B (Molecular Devices, Sunnyvale, CA), filtered at 10 kHz and digitized at 20 kHz using an ITC-16 board (Instru-Tech, Port Washington, NY) and acquired using Axograph X software (Berkeley, CA).

#### **Verification of Slice Health**

All slices evaluated pre- and post-stimulation as in Figure S2 were fixed in formalin, paraffin-embedded, and stained with hematoxylin and eosin by standard protocol. Histological evaluation of cortical slice health was performed by a board-certified neuropathologist (H.V.).

#### **Generation of Conditioned Media from Acute Stimulation**

Thy1::ChR2 or WT mice between the age of 4-7 weeks were briefly exposed to CO<sub>2</sub> and immediately decapitated. Extracted brains were placed in oxygenated high-sucrose solution and sliced in 350- $\mu\text{m}$  sections. Slices were then placed in buffering solution (aCSF) and allowed to recover for at least one hr (as above). After recovery, slices were then moved into fresh aCSF in a 24-well plate and stimulated using a blue-light LED from a microscope objective. The stimulation paradigm mirrored in vivo experiments, using 20-Hz pulses of blue light for 30 s on, 90 s off over a period of 30 min. Surrounding medium was then collected for immediate use or frozen at  $-80^\circ\text{C}$  for future experiments.

#### **Generation of Conditioned Media from 4 Hr Incubation**

As above, WT slices were sectioned on the vibratome and recovered in aCSF solution. Slices were then placed in 24-well plates in oxygenated aCSF in the presence or absence of 1  $\mu\text{M}$  tetrodotoxin (TTX; Tocris Biosciences, Minneapolis, MN) for 4 hr duration. After the 4 hr time period, surrounding media was collected.

### **EdU Incorporation Assay**

8-well chamber slides were coated with poly-L-lysine. Cells were then seeded at 40,000 cells per well and exposed to either blue light-exposed or unexposed aCSF or conditioned media from stimulated or unstimulated Thy1::ChR2 slices or WT slices, or various recombinant proteins (concentrations and conditioning methods vary by assay). 10  $\mu$ M EdU was added to each well. Cells were fixed after 24 hr using 4% paraformaldehyde in PBS and stained using the Click-iT EdU kit and protocol (Invitrogen, Carlsbad, CA). Proliferation index was then determined by quantifying the fraction of EdU labeled cells/DAPI labeled cells using confocal microscopy at 200x magnification, as above.

### **CellTiter-Glo Assay**

To assess overall cell number, 5,000 cells per well of SU-pcGBM2, SU-DIPGIV, SU-DIPGXIII, SU-DIPGVI, SU-GBM034, SU-GBM035, SU-GBM047, SU-GBM052, or SU-AO2 were seeded in minimal growth media in a 96-well plate with either CM from optogenetically stimulated Thy1::ChR2 slices, CM from blue light-exposed WT slices, or aCSF. After 72 hr, CellTiter-Glo reagent (Promega, Madison, WI) was added at a 1:1 ratio. Luminescence was measured after 10 min incubation at room temperature to stabilize signal.

### **Annexin V Apoptosis Assay**

SU-pcGBM2 cells were cultured in minimal growth media together with 50nM NLGN3 recombinant protein (dissolved in PBS) or PBS only as a vehicle control in duplicate for 24 hr. Cells were harvested and FACS analyses of apoptosis were performed using Annexin V-FITC Apoptosis Detection Kit II (556570, BD Biosciences, San Jose, CA) according to the manufacturer's instruction with slight modifications. DAPI was used in combination with Annexin V-FITC to stain the apoptotic cell population. The stained cells were analyzed using a BD Fortessa FACS machine (BD Biosciences, San Jose, CA). The data were analyzed using FlowJo software (FlowJo, LLC).

### **Biochemical Assays**

Fractionation experiments were performed using Amicon ultracentrifugal filters with either 10KDa or 100KDa cutoff membranes (Millipore, Billerica, MA). Conditioned medium from either blue light-exposed WT or optogenetically stimulated Thy1::ChR2 slices was spun through filters at 12,000 rpm for 30 min. All proteins were resuspended in equal volumes of aCSF. Protein denaturation was achieved by boiling the conditioned media from blue light-exposed WT or stimulated Thy1::ChR2 slices for 7 min at 100°C. Nucleic acid degradation was achieved by treatment of the conditioned media with RNase and DNase at a concentration of 2  $\mu$ g/mL and incubated for 1 hr before being added to the cells. All experiments were performed in triplicate.

### **Two-Dimensional Gel Electrophoresis**

Two-dimensional gel electrophoresis (2-D DIGE) and subsequent Protein ID were performed by Applied Biomics, Inc (Hayward, CA).

#### **Preparation of Samples and CyDye Labeling**

Protein sample buffer was exchanged into 2-D cell lysis buffer (30 mM Tris-HCl, pH 8.8, containing 7 M urea, 2 M thiourea and 4% CHAPS). Protein concentration was measured using Bio-Rad protein assay method (Hercules, CA). For each sample, 30  $\mu$ g of protein was mixed with 1.0  $\mu$ l of diluted CyDye, and kept in the dark on ice for 30 min. The labeling reaction was stopped by adding 1.0  $\mu$ l of 10 mM Lysine to each sample, and incubating in the dark on ice for an additional 15 min. The labeled samples were then mixed together. The 2X 2-D Sample buffer (8 M urea, 4% CHAPS, 20 mg/ml DTT, 2% pharmalytes and trace amount of bromophenol blue), 100  $\mu$ l destreak solution and Rehydration buffer (7 M urea, 2 M thiourea, 4% CHAPS, 20 mg/mL DTT, 1% pharmalytes and trace amount of bromophenol blue) were added to the labeling mix to make the total volume of 250  $\mu$ l for the 13-cm IPG strip.

#### **IEF and SDS-PAGE**

After loading the labeled samples, IEF (pH 3-10) was run following the protocol provided by GE Healthcare. Next, the IPG strips were incubated in the freshly made equilibration buffer-1 (50 mM Tris-HCl, pH 8.8, containing 6 M urea, 30% glycerol, 2% SDS, trace amount of bromophenol blue and 10 mg/mL DTT) for 15 min with gentle shaking. Then the strips were rinsed in the freshly made equilibration buffer-2 (50 mM Tris-HCl, pH 8.8, containing 6 M urea, 30% glycerol, 2% SDS, trace amount of bromophenol blue and 45 mg/mL Iodoacetamide) for 10 min with gentle shaking. Next, the IPG strips were rinsed in the SDS-gel running buffer before transferring into 12% SDS-gels. The SDS-gels were run at 15°C until the dye front ran out of the gels.

#### **Image Scan and Data Analysis**

Gel images were scanned immediately following the SDS-PAGE using Typhoon TRIO (GE Healthcare, Waukesha, WI). The scanned images were then analyzed by Image Quant software (version 6.0, GE Healthcare, Waukesha, WI), followed by quantitation analysis using DeCyder software (version 6.5, GE Healthcare, Waukesha, WI). The fold change of the protein expression levels was obtained from in-gel DeCyder analysis.

### **Protein Identification by Mass Spectrometry**

#### **Spot Picking and Trypsin Digestion**

The spots of interest were picked up by Ettan Spot Picker (Amersham BioSciences, Piscataway, NJ) based on the in-gel analysis and spot picking design by DeCyder software. The gel spots were washed a few times, then digested in-gel with modified porcine trypsin protease (Trypsin Gold, Promega, Madison, WI). The digested tryptic peptides were desalted by Zip-tip C18 (Millipore, Billerica, MA).

Peptides were eluted from the Zip-tip with 0.5  $\mu$ l of matrix solution ( $\alpha$ -cyano-4-hydroxycinnamic acid 5 mg/mL in 50% acetonitrile, 0.1% trifluoroacetic acid, 25 mM ammonium bicarbonate) and spotted on the AB SCIEX MALDI plate (Opti-TOF 384 Well Insert, AB SCIEX, Framingham, MA).

#### **Mass Spectrometry**

MALDI-TOF MS and TOF/TOF tandem MS/MS were performed on an AB SCIEX TOF/TOF 5800 System (AB SCIEX, Framingham, MA). MALDI-TOF mass spectra were acquired in reflectron positive ion mode, averaging 4000 laser shots per spectrum. TOF/TOF tandem MS fragmentation spectra were acquired for each sample, averaging 4000 laser shots per fragmentation spectrum on each of the 10 most abundant ions present in each sample (excluding trypsin autolytic peptides and other known background ions).

#### **Database Search**

Both the resulting peptide mass and the associated fragmentation spectra were submitted to GPS Explorer workstation equipped with MASCOT search engine (Matrix Science, Boston, CA) to search the Swiss-Prot database. Searches were performed without constraining protein molecular weight or isoelectric point, with variable carbamidomethylation of cysteine and oxidation of methionine residues, and with one missed cleavage also allowed in the search parameters. Candidates with either protein score C.I.% or Ion C.I.% greater than 95 were considered significant.

### **Spectral Counting and Tandem Mass Tags Proteomic Analyses**

#### **Proteomics Materials**

Ammonium bicarbonate, dithiothreitol (DTT), and iodoacetamide were purchased from Sigma (St. Louis, MO). Sequencing grade modified porcine trypsin was purchased from Promega (Madison, WI). Formic acid, HPLC grade acetonitrile, HPLC grade water and Amino reactive TMT reagents (126 to 131) were purchased from ThermoFisher Scientific (Waltham, MA). BCA protein assay kit was purchased from Pierce (Waltham, MA). C18 Magic bead size 5  $\mu$ m, pore size 300  $\text{\AA}$  was purchased from Michrom Bio-Resources (Auburn, CA). Symmetry 300 C18 5  $\mu$ m NanoEase trap column was purchased from Waters (Milford, MA).

#### **Proteomic Sample Preparation**

Protein digestion and identification by LC-MS/MS was performed as described previously (Faca et al., 2007; Kani et al., 2012). Briefly, sample concentration was estimated by Pierce BCA protein assay (Thermo Scientific, Waltham, MA). Next, in-solution digestion was performed with lyophilized samples that were resuspended, denatured and reduced in 50 mM  $\text{NH}_4\text{HCO}_3$  buffer (pH 8.0) with 10 mM DTT, 0.1% PPS detergent (Agilent Technologies, Santa Clara, CA), for 2 hr at 56°C. The reaction was cooled to room temperature and the sample was alkylated with 50 mM iodoacetamide for 60 min at room temperature in the dark. The resulting mixtures were diluted 6-fold with 50 mM  $\text{NH}_4\text{HCO}_3$  (pH 8.0), and then trypsin was added at a trypsin-to-protein ratio of 1:50 (w/w). The reaction was incubated for 18 hr at 37°C. The digestion was interrupted and acidified by addition of 5  $\mu$ l of 10% formic acid solution. For TMT analysis, Amino reactive TMT reagents (126 to 131, 0.8 mg; Thermo Scientific, Waltham, MA) were dissolved in 41  $\mu$ l acetonitrile, and 10  $\mu$ l of the solution was added to 100  $\mu$ g of peptides. After incubating for 1 hr at room temperature (22°C), the reaction was quenched by adding 8  $\mu$ l of 5% w/v hydroxylamine for 15 min. Following labeling, the sample was combined in equal ratios. The peptide-containing samples were then dried using a speed vacuum concentrator. The samples were reconstituted with 10–20  $\mu$ l of 0.1% (vol/vol) formic acid in water.

#### **Mass Spectrometric Data Acquisition**

Nano-LC-MS/MS was performed using an Eksigent nanoLC 2D system (Dublin, CA) interfaced with a LTQ-Velos-Orbitrap mass spectrometer (Thermo Scientific, Waltham, MA) which is coupled with a CaptiveSpray source (Michrom BioResources, Auburn, CA). The composition of solvent A was 0.1% (v/v) of formic acid in water and solvent B consisted of 0.1% (v/v) of formic acid in HPLC-grade acetonitrile. 10  $\mu$ l of the digested samples were injected using a CTC autosampler (Leap Technologies, Carrboro, NC) onto a Symmetry 300 C18 5  $\mu$ m NanoEase trap column. Samples were loaded onto the trap column at a flow rate of 5  $\mu$ L/min, for 20 min using 0.1% formic acid in water. The peptides were eluted from the trap column and subsequently separated on an IntegraFrit capillary analytical column (150 mm  $\times$  75  $\mu$ m i.d.) packed in-house with Magic C18, using 90 min linear gradient (3%–40% solvent B) at a flow rate of 600 nL/min. The mass spectrometer was operated in a data-dependent MS/MS mode. A single full MS scan, collected in the Orbitrap in profile mode over the mass range of 400–2000 m/z, was accompanied by 10 MS/MS scans, collected in centroid mode in the LTQ, of the 10 most intense peaks. Dynamic exclusion parameters included: repeat count = 1, repeat duration = 30, exclusion list size = 400, exclusion duration = 30 s, and dynamic exclusion width = 1.5 (high and low by mass). For TMT analysis, HCD fragmentation in the Orbitrap was performed.

#### **Peptide and Protein Identification and Quantification**

Acquired data was automatically processed using default parameters, except where noted, by the Computational Proteomics Analysis System V8.2 – CPAS (Eckels et al., 2011; Rauch et al., 2006). The tandem mass spectra were searched against human protein database (UniProtKB) supplemented with sequences for human and bovine trypsin, common contaminants and reverse decoy sequences. The search was performed with X!Tandem (Craig et al., 2004). The mass tolerance for precursor ions was set during the search to 1 AMU with a mass tolerance for fragment ions set to 0.5 Da. However, matches with less than 5 ppm mass accuracy were considered to be false positives and discarded. A fixed modification of 6.020129 mass units was added to lysine residues for database searching to account for incorporation of the heavy lysine isotope. All identifications with a PeptideProphet (Keller et al.,

2002) probability greater than 0.9 were submitted to ProteinProphet (Nesvizhskii et al., 2003) and the subsequent protein identifications were filtered at a 1% error rate with tryptic fragments (1 missed cleavage) with allowance for fixed modification on C = 57.021 and variable modifications on C = -17.027, E = -18.011, K = 6.020, M = 15.995, and Q = -17.027. TMT data were quantified using both ProteomeDiscoverer and Libra.

Proteins selected for subsequent analysis had PeptideProphet and ProteinProphet confidence  $p > 0.99$ , a large number of quantified peptides. Data supporting the change in protein abundance for each of these proteins were manually verified by interrogation of the single ion chromatograms.

Protein quantification by spectral counting was determined using NSAF and  $SI_N$  (Florens et al., 2006; Sardu and Washburn, 2010) as implemented in Crux (McIlwain et al., 2012; McIlwain et al., 2014). To identify proteins with significant fold change between stimulated and unstimulated Thy1::Chr2 conditioned media by spectral counting, we used the EdgeR package (Nikolayeva and Robinson, 2014; Robinson et al., 2010). Peptide spectral counts were modeled as an overdispersed Poisson/negative binomial distribution in which an empirical Bayes procedure was used to moderate overdispersion across each protein. Proteins whose cumulative counts in both conditions were less than 4 were discarded. Using this approach, confidence in a protein's differential abundance in stimulated and unstimulated Thy1::Chr2 conditioned medium is a function of magnitude of difference in normalized counts between conditions and total number of normalized counts. Estimation of absolute abundance of proteins was performed using a weighted spectral count approach as implemented in (Farrar et al., 2011). Spectral counting rests on the observation that the PSM count for a peptide correlates linearly with its molar concentration in the sample (Liu et al., 2004). This approach is essentially a simplification of the APEX method (Vogel and Marcotte, 2008).

Estimation of significance of differential protein abundance in TMT experiments was performed using a generalized linear model approach, as implemented in MSStats (Clough et al., 2012).

### Western Blot Analysis

Briefly, as presented in Figure 5B and 5D, cells were lysed after 1 hr exposure to either 0 nM, 5 nM, 10 nM, or 50 nM recombinant NLGN3 (Origene Technologies, Rockville, MD), using RIPA buffer and protease inhibitors. In Figure 6I, cells were exposed to 50 nM NLGN3 for 12 hr, and then allowed to recover in fresh media for 24 hr. After thorough washing, cells were lysed as above. For all experiments, lysates were incubated on ice for 10 min and then centrifuged for 10 min at 4°C. Protein concentration in the lysate was determined using a Bradford assay. Samples were then normalized to protein concentration, mixed with Laemmli loading buffer (1:4), boiled for 5 min, and loaded onto BioRad Mini-Protean TGX precast gels. Protein was transferred to PVDF membranes and blocked with 5% bovine serum albumin (BSA) in TBST for one hr. Primary antibodies were diluted in 1% BSA/TBST and incubated with the membrane overnight. Antibodies against AKT, phospho-AKT (Ser473), DYKDDDDK Tag, p44/42 MAPK (ERK1/2), phospho-p44/42 MAPK (ERK1/2) (Thr202/Tyr204), 4E-BP1, phospho-4E-BP1 (Thr37/46), PI3K p110a, and mTOR were purchased from Cell Signaling (Danvers, MA) and used at a concentration of 1:1000. Anti-Neuroigin-3 (NovusBio, Littleton, CO) was used at a concentration of 1:300. Anti- $\beta$ -tubulin (Abcam, Cambridge, MA) was used at 1:5000. Secondary anti-rabbit conjugated to HRP (BioRad, Hercules, CA) was then added for one hour (1:1000). Proteins were visualized using Clarity ECL Western Substrate (BioRad, Hercules, CA) and quantified using ImageJ.

### qPCR Analysis

500,000 SU-pcGBM2 or SU-DIPGXIII cells were exposed to either aCSF, 50 nM NLGN3 (Origene Technologies, Rockville), 100 nM BKM120 (SelleckChem, Houston, TX), 100 nM RAD001 (SelleckChem, Houston, TX), 50 nM EGF (Shenandoah, Warwick, RI), or a combination of the above treatments. RNA was extracted using the TRIzol Reagent (Life Technologies, Carlsbad, CA) at either 1 hr (Figure 5A) or 12 hr (Figure 6A-H, S5D-E, S6) after treatment. For qPCR analysis, cDNA was prepared using iScript cDNA Synthesis Kit (BioRad, Hercules, CA). RT-PCR was performed on Eppendorf Mastercycler Realplex2 using Universal SYBR Green Supermix (BioRad, Hercules, CA). Differential expression was determined using the delta CT method. Primers used were as follows:

FOS forward: 5' CCTAACCGCCACGATGATGT 3'; FOS reverse: 5' TCTGCGGGTGAGTGGTAGTA 3'; NLGN3 forward: 5' GGGAG TCCCCTTCTGAAGC 3'; NLGN3 reverse: 5' CCTTCATGGCCACACTGACT 3'; ACTB forward: 5' TGAAGTGTGACGTGGACATC 3'; ACTB reverse: 5' GGAGGAGCAATGATCTTGAT 3'.

### RNA Sequencing

RNA sequencing was performed by Elim Biopharm (Hayward, CA). Total RNA was treated with RiboZero (EpiCentre, Madison, WI) to remove rRNA. The resulting RNA was subject to cDNA synthesis with standard protocol for the first and second strands of cDNA synthesis. Illumina library was prepared from the ds cDNA according to Illumina's standard NGS library preparation method. The libraries were quantified and Q.C.'ed by Qubit, Bioanalyzer, and qPCR. The libraries were then sequenced on Illumina HiSeq2500 (Madison, WI) with 50 bp paired-end read run, generating 179.62M reads. For data analysis, TopHat was used for mapping to the reference genome (hg19(UCSC)), and Cufflinks was used for differential expression analysis.

### Pharmacologic Inhibition

SU-pcGBM2 or SU-DIPGXIII cells were treated with 100 nM BKM120 (SelleckChem, Houston, TX) or 100 nM RAD001 (SelleckChem, Houston, TX) dissolved in DMSO. All experiments using inhibitor treatments used vehicle DMSO treatment as control.

### shRNA-Expressing Lentivirus Preparation and Infection

shRNA expressing lentiviral constructs against human *PIK3CA* and *mTOR* from the RNAi consortium human collection were purchased from Sigma (St. Louis, MO). Lentiviral expressing constructs were co-transfected with packaging plasmids (pDelta 8.92 + VSV-G) into 293T cells to generate lentiviral particles. Lentiviral particles were then concentrated by the polyethylene glycol precipitation method. The precipitated lentiviruses were resuspended in PBS and aliquoted for  $-80^{\circ}\text{C}$  storage. For lentiviral infection, SU-pcGBM2 cells were incubated with shRNA expressing lentivirus; 48 hr post-infection, puromycin (0.5  $\mu\text{g}/\text{ml}$ ) was added to select virally infected cells for further experiments.

### Glutamate Assay

Glutamate concentration in the conditioned media was determined using the reagents and protocols in the Glutamate Assay Kit purchased from Sigma (St. Louis, MO).

### Recombinant Proteins Used

GRP78 (Abcam, Cambridge, MA), BDNF, Brevican, Apolipoprotein E (R&D Systems, Minneapolis, MN), NLGN3 (Origene, Rockville, CA), NRXN1 $\beta$  (R&D Systems, Minneapolis, MN).

### Statistical Analyses

Unpaired, two-tailed Student's *t* tests were used for analysis of tumor burden among experimental groups and change in HGG proliferation index *in vivo*, in NLGN3 necessity and sufficiency experiments, in western blot protein quantification, as well as analysis of change in *FOS* and *NLGN3* expression by qPCR. Group mean differences were otherwise assessed using one-way analysis of variance (one-way ANOVA) with Tukey post hoc tests to further examine pairwise differences. A level of  $p < 0.05$  was used to designate significant differences.

For human genomic analyses, level 3 gene level transcription estimates ( $\log_2$  LOWESS normalized ratio of sample signal to reference signal (cy5/cy3) collapsed by gene) generated on Agilent 244K custom gene expression G4502A\_07\_2 microarrays were downloaded from The Cancer Genome Atlas (TCGA; [www.cancergenome.nih.gov](http://www.cancergenome.nih.gov)). Survival curves were estimated with the use of the Kaplan-Meier product-limit method, and survival distributions were compared across groups with the use of the log-rank test. We performed univariate and multivariate Cox proportional-hazards regression analyses, with overall survival as the dependent variable and *NLGN3* and *NLGN2* expression as the primary predictor. In interpreting hazard ratios, we dichotomized *NLGN3* and *NLGN2* expression at the median. We used an independent-samples Kruskal-Wallis test to compare *NLGN3* expression across various molecular subtypes of glioblastoma. *NLGN3* gene mutation data and cross-cancer *NLGN3* gene alteration data were downloaded from the International Cancer Genome Consortium (ICGC) data portal (<https://dcc.icgc.org>, ICGC Data Release 17, September 12, 2014) and the cBioPortal for Cancer Genomics (<http://cbioportal.org>) (Gao et al., 2013) respectively. Detailed methods for the generation of simple somatic mutations frequencies and for computed functional impact scores using Functional Analysis Through Hidden Markov Models (FATHMM) (Shihab et al., 2013) are available at: <https://docs.icgc.org/methods>.

### SUPPLEMENTAL REFERENCES

- Caretto, V., Sewing, A.C., Lagerweij, T., Schellen, P., Bugiani, M., Jansen, M.H., van Vuurden, D.G., Navis, A.C., Horsman, I., Vandertop, W.P., et al. (2014). Human pontine glioma cells can induce murine tumors. *Acta Neuropathol.* 127, 897–909.
- Clough, T., Thaminy, S., Ragg, S., Aebersold, R., and Vitek, O. (2012). Statistical protein quantification and significance analysis in label-free LC-MS experiments with complex designs. *BMC Bioinformatics* 13 (16), S6.
- Craig, R., Cortens, J.P., and Beavis, R.C. (2004). Open source system for analyzing, validating, and storing protein identification data. *J. Proteome Res.* 3, 1234–1242.
- Eckels, J., Hussey, P., Nelson, E.K., Myers, T., Rauch, A., Bellew, M., Connolly, B., Law, W., Eng, J.K., Katz, J., et al. (2011). Installation and Use of LabKey Server for Proteomics. *Curr. Protoc. Bioinformatics Chapter 13*, Unit13.15.
- Faca, V., Pitteri, S.J., Newcomb, L., Glukhova, V., Phanstiel, D., Krasnoselsky, A., Zhang, Q., Struthers, J., Wang, H., Eng, J., et al. (2007). Contribution of protein fractionation to depth of analysis of the serum and plasma proteomes. *J. Proteome Res.* 6, 3558–3565.
- Farrah, T., Deutsch, E.W., Omenn, G.S., Campbell, D.S., Sun, Z., Bletz, J.A., Mallick, P., Katz, J.E., Malmstrom, J., Ossola, R., et al. (2011). A high-confidence human plasma proteome reference set with estimated concentrations in PeptideAtlas. *Mol. Cell Proteomics* 10, M110 006353.
- Florens, L., Carozza, M.J., Swanson, S.K., Fournier, M., Coleman, M.K., Workman, J.L., and Washburn, M.P. (2006). Analyzing chromatin remodeling complexes using shotgun proteomics and normalized spectral abundance factors. *Methods* 40, 303–311.
- Gao, J., Aksoy, B.A., Dogrusoz, U., Dresdner, G., Gross, B., Sumer, S.O., Sun, Y., Jacobsen, A., Sinha, R., Larsson, E., et al. (2013). Integrative analysis of complex cancer genomics and clinical profiles using the cBioPortal. *Sci. Signal.* 6, p11.
- Kani, K., Sordella, R., and Mallick, P. (2012). Investigation of acquired resistance to EGFR-targeted therapies in lung cancer using cDNA microarrays. *Methods Mol. Biol.* 795, 233–253.
- Keller, A., Nesvizhskii, A.I., Kolker, E., and Aebersold, R. (2002). Empirical statistical model to estimate the accuracy of peptide identifications made by MS/MS and database search. *Anal. Chem.* 74, 5383–5392.
- Liu, H., Sadygov, R.G., and Yates, J.R., 3rd. (2004). A model for random sampling and estimation of relative protein abundance in shotgun proteomics. *Anal. Chem.* 76, 4193–4201.

- McIlwain, S., Mathews, M., Bereman, M.S., Rubel, E.W., MacCoss, M.J., and Noble, W.S. (2012). Estimating relative abundances of proteins from shotgun proteomics data. *BMC Bioinformatics* 13, 308.
- McIlwain, S., Tamura, K., Kertesz-Farkas, A., Grant, C.E., Diamant, B., Frewen, B., Howbert, J.J., Hoopmann, M.R., Käll, L., Eng, J.K., et al. (2014). Crux: rapid open source protein tandem mass spectrometry analysis. *J. Proteome Res.* 13, 4488–4491.
- Nesvizhskii, A.I., Keller, A., Kolker, E., and Aebersold, R. (2003). A statistical model for identifying proteins by tandem mass spectrometry. *Anal. Chem.* 75, 4646–4658.
- Nikolayeva, O., and Robinson, M.D. (2014). edgeR for differential RNA-seq and ChIP-seq analysis: an application to stem cell biology. *Methods Mol. Biol.* 1150, 45–79.
- Paxinos, G., and Franklin, K.B.J. (2008). *The Mouse Brain in Stereotaxic Coordinates*, Third Edition (Academic Press).
- Rauch, A., Bellew, M., Eng, J., Fitzgibbon, M., Holzman, T., Hussey, P., Igra, M., Maclean, B., Lin, C.W., Detter, A., et al. (2006). Computational Proteomics Analysis System (CPAS): an extensible, open-source analytic system for evaluating and publishing proteomic data and high throughput biological experiments. *J. Proteome Res.* 5, 112–121.
- Robinson, M.D., McCarthy, D.J., and Smyth, G.K. (2010). edgeR: a Bioconductor package for differential expression analysis of digital gene expression data. *Bioinformatics* 26, 139–140.
- Sardiu, M.E., and Washburn, M.P. (2010). Enriching quantitative proteomics with SI(N). *Nat. Biotechnol.* 28, 40–42.
- Shihab, H.A., Gough, J., Cooper, D.N., Stenson, P.D., Barker, G.L., Edwards, K.J., Day, I.N., and Gaunt, T.R. (2013). Predicting the functional, molecular, and phenotypic consequences of amino acid substitutions using hidden Markov models. *Hum. Mutat.* 34, 57–65.
- Vogel, C., and Marcotte, E.M. (2008). Calculating absolute and relative protein abundance from mass spectrometry-based protein expression data. *Nat. Protoc.* 3, 1444–1451.

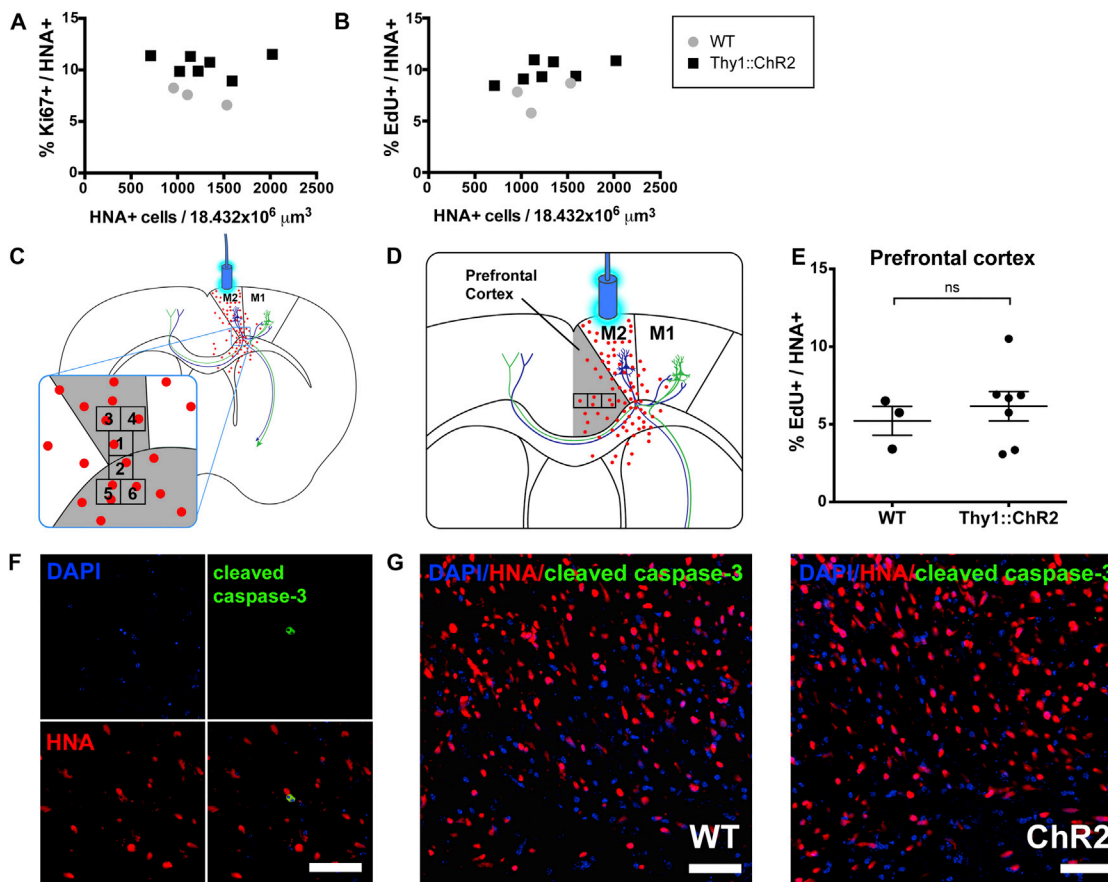


**Figure S1. Neuronal Activity Promotes Glioma Proliferation within the Active Circuit, Related to Figure 1**

(A and B) Equivalent xenografted cell density in the premotor circuits of both genotypes at the time of optogenetic stimulation. Given that the density of a tumor can affect its mitotic rate, the density of tumor cells within the optogenetically stimulated premotor circuit in Thy1::ChR2;NSG (black squares) and identically-manipulated WT;NSG (gray circles) mice was assessed to demonstrate equivalent tumor engraftment between the two genotypes at the time of optogenetic stimulation. The proliferation index of xenografted human nuclear antigen<sup>+</sup> (HNA<sup>+</sup>) tumor cells at an acute (24 hr) time point, measured by co-labeling with Ki67 (A) or EdU (B) and as also depicted in Figure 1D, is expressed as a function of tumor cell density within the total quantified area of the premotor circuit as indicated below in panel (C). Note that 24 hr is earlier than the ~2 day doubling time for this patient-derived cell culture, and thus no change in cell density resulting from the activity-regulated increase in proliferation rate would be expected at this early time point. Tumor cell density did not differ between genotypes in the acute period following a single session of optogenetic stimulation, indicating well-matched tumor density in both groups ( $n = 7$  Thy1::ChR2,  $n = 3$  WT;  $p = 0.74$  by unpaired two-tailed Student's *t* test).

(C) Schematic illustrating the location of 6 selected quantification fields for live cell counting at 400x magnification. Fields were systematically selected as depicted within the active circuit in premotor cortex and subjacent white matter, using the cingulum bundle as an anatomic landmark. Field selection and quantification was repeated for each of 3 consecutive 40- $\mu$ m slices of a 1 in 6 series selected for closest proximity to the orthotopic implantation site in the coronal plane by our selected stereotactic xenograft coordinates.

(D and E) The effects of activity on glioma cell proliferation are localized to the active circuit. Xenografted glioma cells infiltrating the neighboring prefrontal cortex (highlighted in gray (D)), outside of the region of light stimulation and not a target of premotor circuit projections, do not exhibit an increase in proliferation index (E) in Thy1::ChR2;NSG mice compared to WT;NSG mice as assessed by incorporation of EdU delivered at the time of a single optogenetic stimulation session and assessed 24 hr later ( $n = 7$  Thy1::ChR2,  $n = 3$  WT;  $p = 0.57$  by unpaired two-tailed Student's *t* test).

(F and G) Confocal micrographs demonstrating cleaved caspase-3 (green) immunohistochemistry in pHGG xenografts (HNA<sup>+</sup> = red; DAPI = blue). Only rare cleaved caspase-3<sup>+</sup> cells were detected (F). (G) Representative images from optogenetically stimulated ("ChR2") or identically manipulated WT premotor area (cortex and subjacent corpus callosum) illustrates little to no apoptotic cell death in either group.

Scale bars = 50  $\mu$ m. Data presented as mean  $\pm$  SEM. n.s. indicates  $p > 0.05$ .

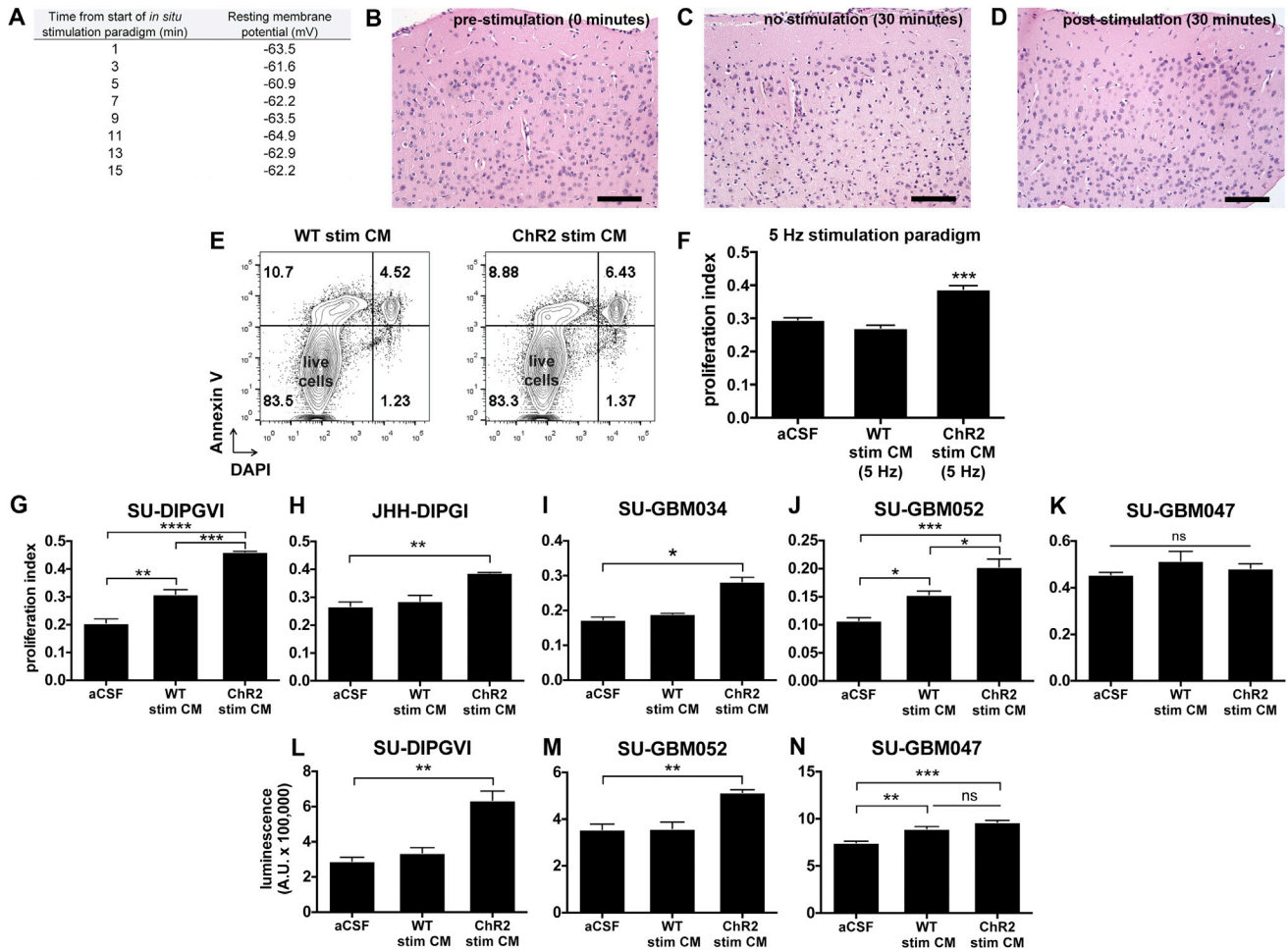


**Figure S2. In Situ Optogenetic Stimulation Paradigm Reveals Activity-Regulated Secreted Glioma Mitogens, Related to Figure 2 and Table S1**

(A-D) Acute cortical slice health. The *in situ* optogenetic stimulation paradigm does not adversely affect slice health, as evidenced electrophysiologically and histologically. (A) Constant resting membrane potential of layer V cortical projection neurons documented at regular 90 s intervals in between 30 s periods of *in situ* optogenetic stimulation with 473-nm light at 20 Hz. B-D) H&E micrographs of cortical slices prior to optogenetic stimulation (B), with no optogenetic stimulation at 30 min (C) and after the 30 min optogenetic stimulation paradigm (D). Histological review by a board-certified neuropathologist (H.V.) revealed no evidence of neuronal injury.

(E) Annexin V FACS analysis. After 24 hr exposure to PBS or active CM, SU-pcGBM2 cells were stained with DAPI and Annexin V-FITC to detect cell death by FACS analysis. Annexin V<sup>+</sup> cells are shown on the y axis and DAPI<sup>+</sup> cells on the x axis. Live Annexin V<sup>-</sup>/DAPI<sup>-</sup> cells are shown in the lower left quadrant, pre-apoptotic Annexin V<sup>+</sup>/DAPI<sup>-</sup> cells are shown in the left upper quadrant and dead Annexin V<sup>+</sup>/DAPI<sup>+</sup> cells are shown in the right upper quadrant of the contour plots. FACS analyses repeated in biological duplicate.

(F) Proliferation index of pHGG cells (SU-pcGBM2) exposed to CM from Thy1::ChR2 cortical slices optogenetically stimulated at 5 Hz, CM from WT cortical slices exposed to blue light at 5 Hz, or plain media (aCSF), determined by the EdU assay.

(G-K) Effect of active CM on the proliferation of additional cell lines as measured by the EdU assay, including DIPG cultures (SU-DIPGVI, JHH-DIPGI), adult glioblastoma cultures (SU-GBM034, SU-GBM052) and a culture from a young adult epithelioid glioblastoma (SU-GBM047).

(L-N) Effect of active CM on the overall growth of additional cell lines as measured by the CellTiter-Glo assay. See also Table S1 for the clinical and molecular characteristics of the cultured tumors.

Data presented as mean  $\pm$  SEM. All experiments performed in three biological replicates and analyzed by one-way ANOVA with Tukey's post hoc tests to examine pairwise differences unless otherwise stated. \* $p < 0.05$ , \*\* $p < 0.01$ , \*\*\* $p < 0.001$ , \*\*\*\* $p < 0.0001$ . n.s. indicates  $p > 0.05$ .

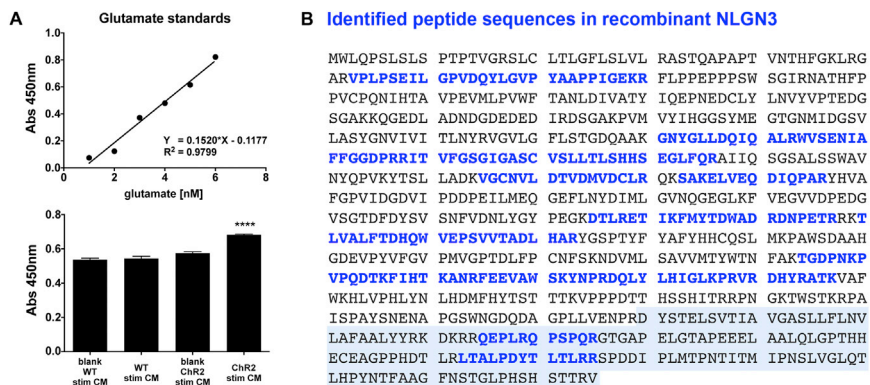


**Figure S3. Conditioned Medium from Optogenetically Stimulated Cortical Slices Contains Secreted Nlgn3 and Little Glutamate, Related to Figure 3**

(A) The glutamate concentration was assayed in CM from optogenetically stimulated Thy1::Chr2 cortical slices (active CM) or from identically-manipulated WT cortical slices. The standard curve (top panel) illustrates calibration of the assay. Low glutamate levels were detected in active CM samples (bottom panel). Data presented as mean  $\pm$  SEM;  $n = 3$  replicates; \*\*\*\* $p < 0.0001$  by one-way ANOVA.

(B) Mass spectrometric analysis confirms the identity of the full-length recombinant NLGN3. Identified peptide sequences are shown in blue. Note identified peptide sequences in the C-terminal endodomain region (transmembrane domain + intracellular domain) of the recombinant protein (shaded gray), not observed in the secreted form of the protein found in active CM (see Figure 3H).

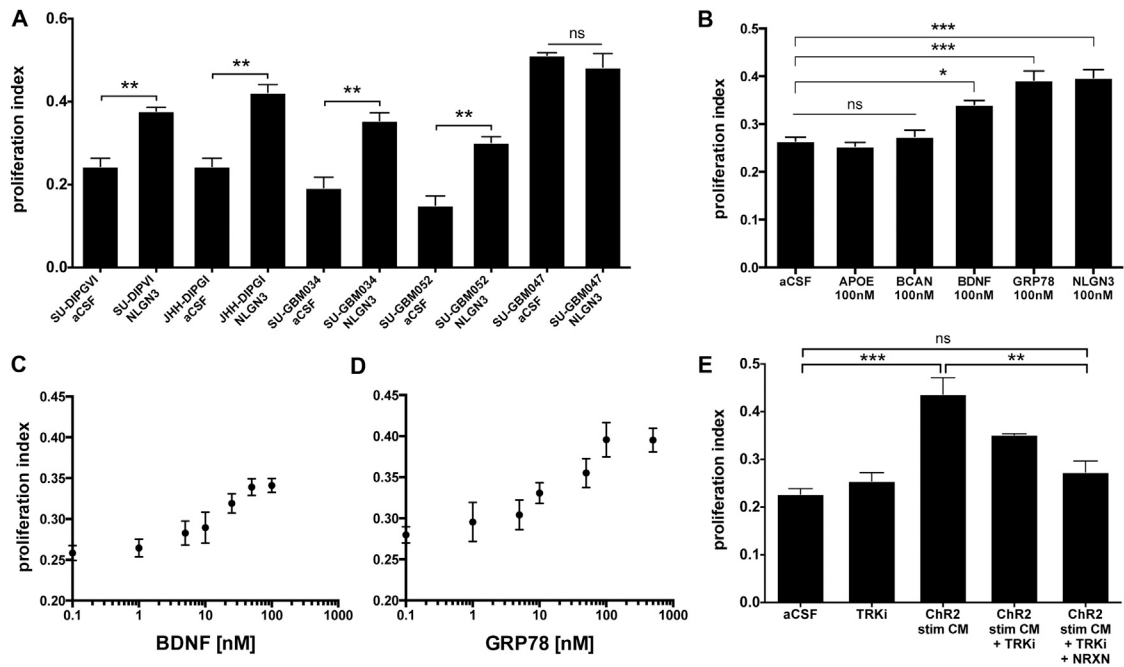


**Figure S4. Activity-Regulated Secretion of Glioma Mitogens, Related to Figure 4**

(A) NLGN3 promotes proliferation in a broad range of HGG cultures. Additional cell lines, including DIPG (SU-DIPGVI, JHH-DIPGI), adult glioblastoma (SU-GBM034, SU-GBM052) and epithelioid BRAF<sup>V600E</sup> glioblastoma (SU-GBM047) were exposed to 50nM recombinant NLGN3. After 24 hr exposure, all cell lines were evaluated with the EdU assay to determine proliferation index (unpaired two-tailed Student's *t* tests).

(B) Activity-regulated candidate mitogens identified by proteomic analyses of cortical slice CM were tested. Pediatric HGG cells (SU-pcGBM2) were exposed to recombinant versions of the candidate proteins at 100 nM concentration for 24 hr, and proliferation index was determined as the fraction of DAPI<sup>+</sup> cells co-expressing EdU. Of these candidates, NLGN3, BDNF and GRP78 were found to promote glioma cell proliferation relative to aCSF control (one-way ANOVA was used with Tukey's post hoc tests to examine pairwise differences).

(C and D) 7-point dose curves plot proliferation index measured at 24 hr following exposure of SU-pcGBM2 cells to recombinant BDNF (C) or GRP78 (D) at concentrations ranging from 0 – 100 nM (C) or 0 – 500 nM (D).

(E) BDNF receptor TRKB inhibition. The TRKB inhibitor ANA12 was used to determine the magnitude of BDNF contribution to the proliferative effect of the active CM. To that end, SU-pcGBM2 cells were exposed to active CM, 100nM TRK inhibitor ANA12 (TRKi), and 500nM NRXN, alone or in combination. Proliferation was evaluated using the EdU assay and analyzed using a one-way ANOVA with Tukey's post hoc tests to examine pairwise differences.

All experiments were performed in three biological replicates. Data presented as mean  $\pm$  SEM. \**p* < 0.05; \*\**p* < 0.01; \*\*\**p* < 0.001; n.s. indicates *p* > 0.05.

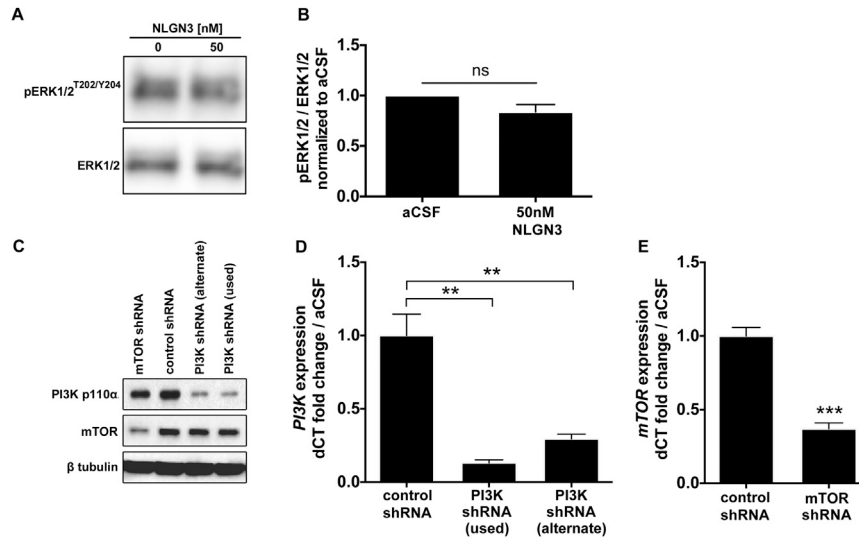


**Figure S5. Evaluation of MAPK Pathway and Validation of *PI3K-mTOR* shRNA Constructs, Related to Figure 5**

(A) Western blot analysis of phosphorylated ERK1/2 (Thr202/Tyr204) and total ERK1/2 in SU-pcGBM2 cells after exposure to either aCSF or NLGN3 (50 nM). Representative Western blot shows phosphoERK1/2<sup>T202/Y204</sup> top panel; total ERK1/2 bottom panel.

(B) Phosphorylated ERK1/2 levels were normalized to total ERK1/2 levels. No significant change in ERK1/2 phosphorylation (Thr202/Tyr204) was seen with exposure to NLGN3 (n = 3 biological replicates; unpaired two-tailed Student's t test).

(C) Representative Western blots confirming the shRNA knockdown of PI3K and mTOR. From left, first lane represents cells exposed to *mTOR* shRNA knockdown construct, second lane represents cells exposed to scrambled shRNA control, third and fourth lanes represent cells exposed to *PI3K* knockdown constructs. Top row probed with anti-PI3K antibody, middle row probed with anti-mTOR antibody, bottom row probed with anti-β-tubulin antibody.

(D and E) *PI3K* and *mTOR* mRNA expression as quantified by qPCR in order to verify *PI3K* and *mTOR* knockdown in various constructs. “PI3K (used)” represents construct used in the Figures 5 and 6. “PI3K shRNA (alternate)” represents an additional construct used to verify observation and to control for off-target effects (see also Figure S6).

All experiments performed in three biological replicates and analyzed by unpaired two-tailed Student's t test. Data presented as mean ± SEM. \*\*p < 0.01, \*\*\*p < 0.001. n.s. indicates p > 0.05.

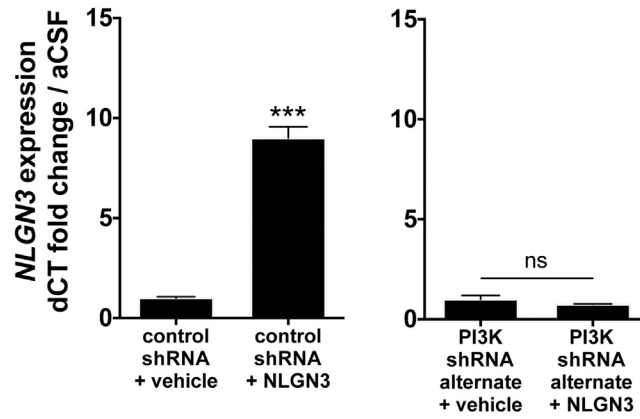
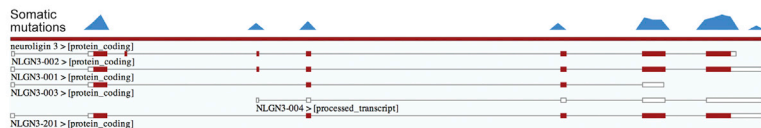


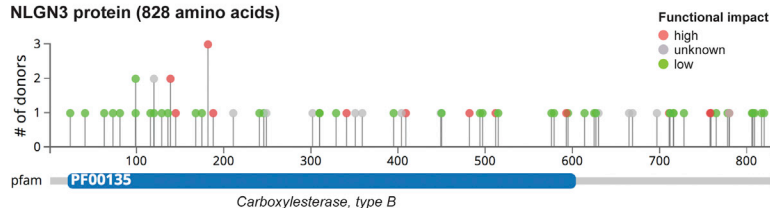
**Figure S6. Alternate *PI3K* shRNA Construct Verifies the Role of *PI3K* in Feedforward *NLGN3* Expression, Related to Figure 6**

Use of an alternate shRNA construct for *PI3K* knockdown to further control for off-target effects verifies that *PI3K* knockdown blocks NLGN3-induced *NLGN3* expression in glioma cells. *NLGN3* gene expression was determined by qPCR following exposure to 50 nM recombinant NLGN3 in glioma cells infected with an alternate *PI3K* shRNA knockdown construct or scrambled shRNA control (shRNA control data presented in Figure 6C are repeated here (left graph) for reference. See also Figure S5C and S5D). Experiments performed in three biological replicates and analyzed by unpaired two-tailed Student's t test. Data presented as mean  $\pm$  SEM. \*\*\* $p < 0.001$ . n.s. indicates  $p > 0.05$ .

**A** *NLGN3* gene (chrX:70364681-70391051)



**B** *NLGN3* protein (828 amino acids)



**C** *NLGN3* gene alterations across cancer types

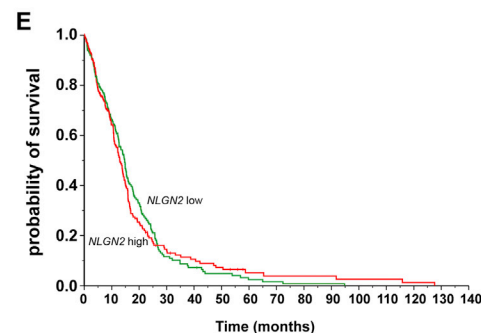
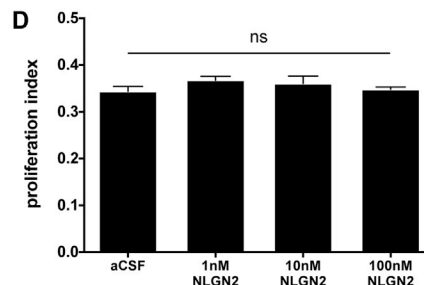
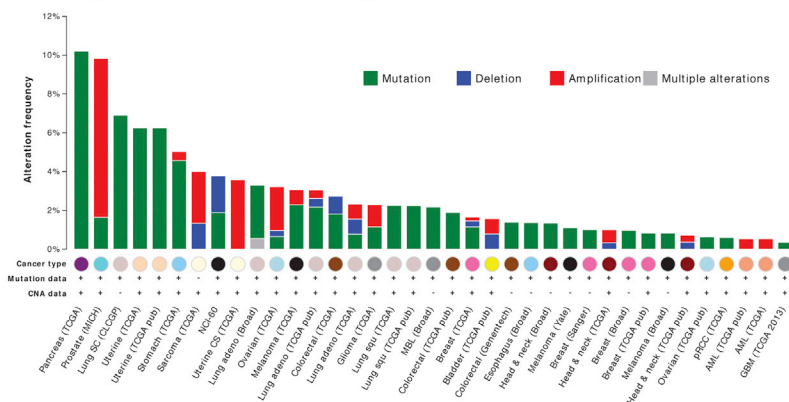


**Figure S7. Genomic Aberrations in the *NLGN3* Gene in Human Cancer and *NLGN2* Control Data, Related to Figure 7**

(A) Structure and reference sequence of human *NLGN3* transcripts with frequency mapping of mutations, consisting mostly of single base substitutions, across seven coding exons.

(B) Mapping of these mutations throughout all seven *NLGN3* exons and across the entire 828-amino acid *NLGN3* sequence with predictions of potential functional impact.

(C) Frequency of *NLGN3* gene alterations, involving mutations and copy number variations, across various cancer types demonstrates the presence of mutations and/or copy number variations (frequency: 0.4%–10.2%) in 37 of 69 cancer studies involving 17,584 tumors curated in the cBioPortal for Cancer Genomics. The presence of *NLGN3* mutations in various cancers supports a potential tumor-promoting role of *NLGN3* in human carcinogenesis, yet their paucity in brain tumors suggests primarily transcriptional or post-transcriptional mechanisms of *NLGN3* deregulation in glial brain tumors.

(D and E) Neuroligin-2 (*NLGN2*) does not promote glioma cell proliferation and does not correlate with patient overall survival. (D) Pediatric HGG cells (SU-pcGBM2) were exposed to recombinant *NLGN2* at 1, 10 or 100 nM concentration for 24 hr, and proliferation index was determined as the fraction of DAPI<sup>+</sup> cells co-expressing EdU. No effect of *NLGN2* on pHGG cell proliferation was observed (one-way ANOVA,  $n = 3$ ). Data presented as mean  $\pm$  SEM. n.s. indicates  $p > 0.05$ . (E) A two-class model stratified by median *NLGN2* expression in 429 GBM cases with molecular subtype data from the TCGA (<http://cancergenome.nih.gov>). Mean survival did not differ between the cohorts of patients whose tumors exhibited above- or below-median *NLGN2* expression ( $p = 0.795$  by the log-rank test).